NTNU

Norwegian University of
Science and Technology

Experimental Study of High-Pressure Gas Injection Using Optical Methods

Jens Kristian Myhrer Bredahl

Preface

This work is a masters thesis in marine engineering at the Department of Marine Technology, NTNU. It was written during the spring semester of 2018 and represents the work of a full semester. Conducting the research has been a challenging, yet educational experience. During the course of this semester a number of delays and obstacles were encountered, as research on gas injection had never been done in the laboratory before. This made the process of procuring the necessary parts, assembling a working experimental setup and performing experiments more time-consuming than expected, but in the end some good results were achieved, thanks to many helpful partners.

I would like to extend my gratitude to the following people:

Vladimir Krivopolianskii, PhD Candidate and co-supervisor, for providing guidance, consultation and instruction throughout the entire process and for always taking the time to help me. Your help with installing equipment, preparing the test setup and analyzing the results has been invaluable.

My academic supervisor, Professor Sergey Ushakov, for providing the assignment and for giving me the opportunity to work on such a fascinating subject.

Frode Gran, Senior Engineer at the Department of Marine Technology at NTNU, for providing help by designing the control system and for installation of sensors crucial for the work.

Kristian Minde, Department Engineer at the Department of Marine Technology at NTNU, for assistance and production of components critical for the performance of the experiments conducted.

The entire team working in the electrical and construction labs at the Center of Marine Technology for always lending a helping hand whenever it was needed.

My family for supporting me throughout the entire course of my education.

Trondheim, 11.06.2018

Jens K. M .Bredahl

Summary

This thesis first presents the role of LNG as a potential means to reduce marine emissions and get international shipping into compliance with new regulations set by regulatory authorities. An overview of different gas engine concepts with their merits and limitations is also presented.

An experimental study have been conducted at SINTEF Ocean's engine laboratory in order to determine the operational profile of a prototype gas injector. Special focus was put on determining the injector discharge coefficient and macroscopic gas jet characteristics. Experiments with both steady state flow conditions and dynamic rapid burst injections were performed for a wide range of injection pressures. Five different injector nozzles, three circular nozzles with diameters of 1.48mm, 2.04mm and 2.88mm, and two specially designed non-circular nozzles were used. This allowed for the study of the effect of nozzle geometry on the injection. The optical techniques Schlieren and Background-Oriented Schlieren were used to study the injection of high-pressure gas into a constant volume combustion chamber. For these experiments the injection pressures used was 381bar and 218 bar. For half of the tests the chamber pressure was atmospheric, for the other half the chamber was pressurized to 20 bar using nitrogen.

The results from the steady-state experiments show that the larger nozzles experienced more losses. The discharge coefficient for the fully opened injector in the choked flow region was: 0.96, 0.78 and 0.44 for the circular nozzles with diameter 1.48mm, 2.04mm and 2.88mm respectively. The non-circular nozzles had a similar, but slightly lower discharge coefficient than the smallest circular nozzle, which had the same area. The rapid burst tests showed the effect of the transient phase of needle lift on the discharge coefficient. Significantly lower discharge coefficient were obtained for all nozzles during these tests, indicating more losses.

A model for predicting the mass delivery of the injector was devised. This model showed that mass delivery was linearly dependent on the injection pressure, and the nozzle that provided most injected mass was the 2.04mm diameter circular nozzle.

The Background-Oriented Schlieren study yielded unsatisfactory results due to difficulties setting proper boundary conditions, but showed potential for further improvement.

Due to the choking phenomenon, which limits the gas jet speed to sonic velocity, increased injection pressure did not seem to significantly increase jet propagation speed. Increased chamber pressure resulted in a significantly slower jet propagation with a more profound density gradient, seen as a starker contrast in the Schlieren images. The smaller nozzles provided faster jet propagation than the larger ones during the transient phase, but for the fully developed jets the circular nozzles showed the largest maximum penetration lengths.

A relation between nozzle size and gas jet cone angle was discovered, where larger nozzle area yielded a wider jet cone angle. No conclusive results were obtained regarding the effect of injection- or ambient pressure on jet cone angle.

Sammendrag

Denne oppgaven presenterer først flytende naturgass' rolle som en potensiell måte å redusere marine utslipp og få internasjonal skipsfart til å samsvare med nye reguleringer fastatt av myndigheter. En oversikt over forskjellige gassmotorkonsepter med deres fordeler og ulemper er også presentert.

En eksperimentell studie ble utført på SINTEF Oceans motorlaboratorium for a bestemme operasjonsprofilen til en gassinjektor prototype. Spesielt fokus ble lagt på å bestemme dischargekoeffisient og makroskopiske gassjetkarakteristikker. Eksperimenter med både stabile strømningsforhold og hurtige serier med injeksjoner ble gjort for en rekke forskjellige injeksjonstrykk. Fem forskjellige dyser, tre sirkulære dyser med diameter 1.48mm, 2.04mm og 2.88mm, og to spesialdesignede ikke-sirkulære dyser ble brukt. Dette muliggjorde studier av dysegeometriens effekt på injeksjonen. De optiske metodene Schlieren og Background-Oriented Schlieren ble benyttet for å studere injekson av høyttrykk gass inn i et konstant-volum forbrenningskammer. Injeksjonstrykkene brukt i disse eksperimentene var 381bar og 218 bar. Halvparten av testene ble utført med atmosfærisk trykk i kammeret og for den andre halvparten ble kammeret trykksatt til 20 bar ved å fylle det med nitrogen.

Resultatende fra de stabile eksperimentene viser at større dysene opplevde større tap. Dischargekoeffisienten for den fullt åpne injektoren i det strupede strømningsområdet var: 0.96, 0.78 og 0.44 for de sirkulære dysene med diameter 1.48mm, 2.04mm and 2.88mm. De to ikke-sirkulære dysene hadde lignende, men litt lavere dischargekoeffisienter enn den minste sirkulære dysen med samme dyseareal. De hurtige seriene viste effekten av den transiente fasen med nålløft på dischargekoeffisienten. Betydelig lavere dischargekoeffisient ble oppnådd for samtlige dyser, hvilket indikerer større tap.

En model for å predikere levert masse fra injektoren ble utviklet. Modellen viste at injisert masse er lineært avhengig av injeksjonstrykk, og dysen som ga mest masse var den sirkulære dysen med diameter 2.04mm.

Resultatene fra Background-Oriented Schlieren studien var ikke tilfredsstillende, da det var vanskelig å sette gode grensebetingelser, men den viste potensiale for videre forbedring.

På grunn av struping som begrenser gassjetens hastighet til den lokale soniske hastigheten, ga ikke økt injeksjonstrykk noen betydelig økt jethastighet. Økt kammertrykk resulterte i en betydelig tregere jet med en tydeligere tetthetsgradient, som kan sees som mørkere kontrast på Schlierenbildene. De mindre dysene hadde raskere jetforplantning under den transiente fasen, men for den fullt utviklede jeten viste de sirkulære dysene lengst pentreringslengde.

En sammenheng mellom dysestørrelse og gassjetvinkel ble observert, der større dyseareal ga bredere vinkel. Ingen konklusive resultater ble oppnådd angående effekten av injeksjonsog kammertrykk på jetvinkel.

Contents

List of Figures

List of Tables

Nomenclature

$\dot{m}$ Mass flow rate

ϵ Light refraction angle

Γ Penetration constant

κ Specific heat ratio

ϕ Fuel-air equivalence ratio

ρ Density

A Area

a Sonic velocity

C_D Discharge Coefficient

c_p Specific heat capacity at constant pressure

c_v Specific heat capacity at constant volume

d_n Nozzle diameter

f Gas flow velocity

K Refractive index multiplier

k Gladstone-Dale coefficient

l Needle lift

n Refractive index

P Pressure

R Gas constant

r Radius

s Cone slant height

S_t Penetration length

T Temperature

t Time

U_n Nozzle exit velocity

V Gas flow velocity

v Sampling frequency

List of Abbreviations

BOS	Background-Oriented Schlieren
ECA	Emission Control Area
EGR	Exhaust Gas Recirculation
HPDF	High-Pressure Dual-Fuel
IMO	International Maritime Organization
LBSI	Lean-Burn Spark Ignition
LED	Light-Emittind Diode
LNG	Liquefied Natural Gas
LPDF	Low-Pressure Dual-Fuel
NPR	Nozzle Pressure Ratio
PM	Particulate Matter

Chapter 1

Introduction

Emissions and pollution from the maritime industry is a subject of increased focus, and authorities are imposing ever stricter regulations. These shifts bring with them a need for innovation and the development and implementation of new solutions. Phasing out conventional marine fuels with alternative fuels with a cleaner emission profile is one of the ways to reduce emissions and stay within compliance of regulations. Liquefied natural gas (LNG) is one of the most promising options both in terms of economic viability and availability. In later years the number of ships using natural gas as primary energy carrier has increased greatly.

An LNG engine concept that is not very widespread, but shows a lot of potential is the high-pressure dual-fuel (HPDF) engine. The benefits in the form of emission reduction and efficiency increase does, however come with a number of challenges not present in other engines. The operational profile of a dual-fuel engine is more complex than for a conventional marine diesel engine. Operation ranges from being almost entirely gas powered with only using a small pilot injection of diesel, constituting $< 2\%$ of the energy, all the way to 100% diesel operation. The fact that the HPDF is a direct injection engine entails that there is short time for mixture formation in the combustion chamber which makes understanding the characteristics and fluid interaction of the injected gas jet crucial. These complexities and challenges along with the fact that the research on high-pressure gas injection is quite limited make it a relevant field of study.

1.1   Background

A prototype gas injector designed for conducting tests of high-pressure natural gas injection has been made for testing in the engine lab at SINTEF Ocean. This makes it possible to perform experiments charting the injection- and combustion process of high pressure dual fuel engines in the laboratory. As this injector is brand new and not made from standardized specifications, the injection characteristics and operational profile had to be determined.

A preliminary study was conducted as a specialization project thesis during the fall of 2017. During this the work on this project a study of some of the injection characteristics of the injector was conducted, but the results obtained did not provide satisfying stability and had a somewhat limited data basis. Therefore some of the experiments conducted

have been repeated in order to establish a more robust data basis and more stringent testing protocols. A basis for much of the study on the state of the art was also laid during the work on this specialization project.

1.2   Scope of Work

Summed up, the scope of the work conducted in this study is as follows:

1. Assist in the modification of the laboratory and aid in outfitting it with new equipment.

2. Carry out a background study:

   - Give an introduction to the subject of marine emissions, regulations and reduction measures.
   - Present status and viability of LNG as fuel.
   - Present current natural gas engine technology.

3. Devise experiments designed to obtain relevant data.

4. Perform high pressure gas injection testing using different imaging techniques.

5. Analyze the results.

   - Analyze images to obtain gas jet geometry.
   - Present evaluation of the data and compare it to relevant studies.

1.3   Modifications to the Laboratory

The combustion laboratory has never before been used for testing with gaseous fuels, so in order to conduct the desired research a multitude of modifications and additions had to be done to the existing test setup. New components had to be procured and installed, new analysis tools had be created and existing tools had be modified. This has taken up a considerable amount of time at the cost of time available for conducting experiments and post-processing of results. There is still a ways to go if perfect test conditions are to be achieved.

The most important new feature in the lab is perhaps the prototype gas injector. The operation of this injector have been challenging. Numerous leaks that have had to be fixed and determining the behavior and dynamics has been quite difficult.

In order to obtain the high pressures required for the desired research, a gas pressurization system had to be implemented. An attempt was made to use a piston booster-pump utilizing the existing liquid fuel pressurization system, but this resulted in leaks between the gas and liquid systems. Eventually, a compressor was obtained from another laboratory and the installation of necessary piping and was done. This addition to the laboratory

inventory will enable injection of gaseous fuels at pressures high enough to be representative of a high-pressure direct-injection gas engine.

For the Background-Oriented Schlieren (BOS) experiments, some new additions to the optical setup was acquired. Among others a new photo-electric diode capable of emitting significantly more intense light than previously used light sources in the lab. The implementation of this took considerable effort as the timing of the camera shutter and light pulses had to be synchronized using an oscilloscope to get even lighting in all frames in a series of images. New lenses were also acquired for this test setup.

Control systems and sensors for the new components were also designed and installed with the help of senior engineer Frode Gran.

These modifications opens the door for a wide span of new research opportunities in the laboratory.

1.4   Structure of the Report

Chapter 1 serves as an explanation on why the study of high pressure gas injection is a relevant topic, gives a brief overview of the previous work and sums up some of the modifications that has been done to the laboratory during the work on the thesis.

Chapter 2 briefly covers the topic of marine emissions, emission regulations and emission reduction measures.

Chapter 3 provides a short overview of current marine natural gas engine technology.

Chapter 4 describes some important characteristics of the gas jet and injector such as gas jet geometry and injector discharge coefficient.

Chapter 5 explains the imaging techniques utilized in this study in short.

Chapter 6 lists the research equipment used in this study and provides some additional information about said equipment.

Chapter 7 aims to explain the test procedure, define the test parameters and describe the analysis methods used to obtain the results.

Chapter 8 includes the presentation and discussion of the results obtained in the study.

Chapter 9 contains the conclusions and the authors recommendations for further work.

Chapter 2

Emission Concerns

In order to establish and maintain the current standard of living in the first world a tremendous increase in energy production has had to take place. We expect electricity in our power outlets, our houses to be warm, our devices to be powered and our goods to be delivered on time. The vast majority of the energy required to facilitate this standard comes from the combustion of fossil fuels [1]. Since the dawn of the industrial revolution and the modern era the emissions from the combustion of said fossil fuels have skyrocketed.
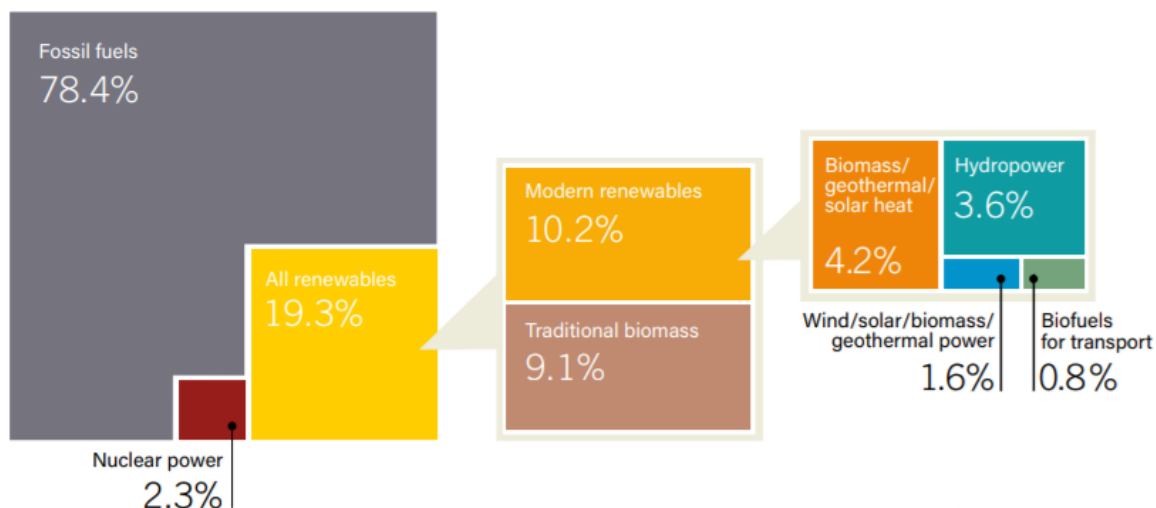
Figure 2.0.1: World energy consumption by source, 2015

Shipping is the most energy efficient mode of transportation in terms of emissions pr. ton goods transported, but for a long time the maritime transportation sector was under-regulated and free to consume cheap, low-quality bunker fuel with a terrible emission profile. Given that nearly 70% of shipping emissions occur less than 400km from land it has the potential to emit considerable pollution in coastal communities [2]. These emissions have caused a number of severe adverse effects on the environment and on public health.

2.1 Greenhouse Gases

Greenhouse gases absorb thermal energy and trap heat in the atmosphere, and the production of greenhouse gases is inherent in the combustion of fossil fuels. Man-made global warming is a growing concern, as the worlds temperatures are rising and extreme weather is more prominent than ever.
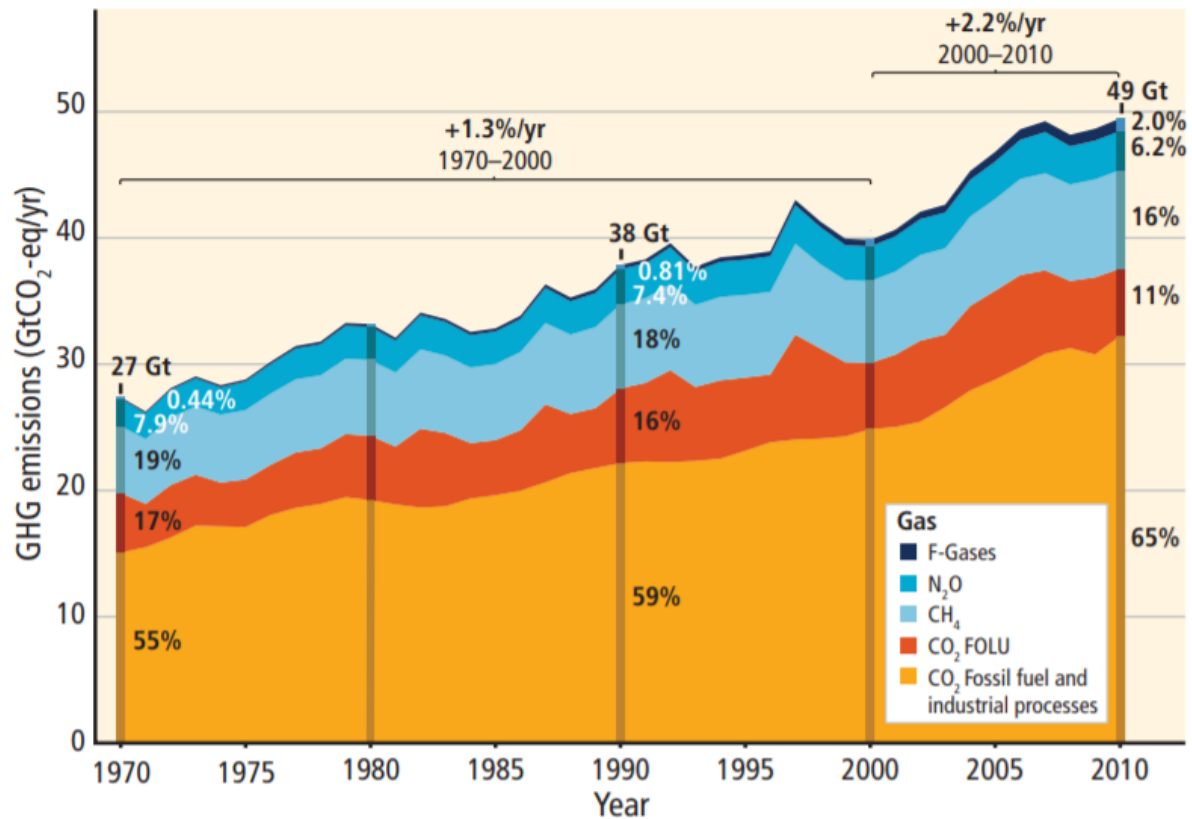
Figure 2.1.1: Total annual anthropogenic GHG emissions by gases 1970–2010

At the global scale the most impactful anthropogenic greenhouse gases are carbon dioxide (CO_2) methane, nitrous oxide and flourinated gases. Of these, CO_2 is by far the most responsible for the increased temperatures. With its radiative forcing constituting 83% of the total anthropogenic radiative forcing(from 1750 to 2011)[3] it has had a significant effect on the climate. Radiative forcing is defined as the difference between energy absorbed by earth and the energy radiated back into space, given in Watts pr. square meter of the earth's surface. International shipping was in 2012 estimated to produce 2.2% of the global CO_2 emissions[4] making it a modest contributor to the total CO_2 emissions. Yet a global approach to emission reduction from all contributors is necessary if the effects of global warming is to be halted, and sea transport is growing each year following the growth in world trade.

2.2 Particulate Matter

By definition, the particle pollution, also called particulate matter or PM, is the term for a mixture of solid particles and liquid droplets suspended in the air[5]. A distinction is

made between primary and secondary PM. Primary PM is formed during the combustion process and during exhaust gas ambient dilution and consists primarily of unburnt carbon, metal oxides and sulfates. Secondary PM is formed later on as sulphur dioxide, nitrogen oxides and ammonia reacts to form ammonium sulphates and nitrates. Marine particulate emissions mainly come from the fuel, lubrication oil and metal residue from mechanical wear and tear on moving components.

PM emissions impact both health and environment. It has been proven that PM emissions are clearly linked to severe health deficiencies such as cardiac arrhythmia, exacerbate asthmatic symptoms and increase both lung and vascular inflammation. These effects are so severe that it has been estimated to cause approximately 60 000 premature deaths annually[2]. The maritime industry is responsible for a large proportion of the world's particle pollution with an estimated total emission of 1.67 million metric tons (Tg) of particulate matter (PM) with aerodynamic diameters of 10 µm or less (PM_{10}) in 2003 [6]. In spite of this, no concrete regulations are in place to limit PM emissions.

2.3 Sulphur Oxides

The emission of sulphur oxides, SO_x, is also a significant problem in the maritime sector. SO_x is formed as sulphur in the fuel is oxidized during combustion. Almost all of the sulphur in the fuel will react with oxygen during combustion so the sulphur content of the fuel is a direct indication to how much sulphur oxides will be emitted during operation.

Emissions of SO_x can react to form sulphuric acid or particulates, which in turn can cause respiratory problems, devastate fragile eco-systems and damage or destroy buildings and monuments. The maritime sector is a large contributor to the world's SO_x emissions, with international shipping alone producing 13% of the world's anthropogenic SO_x in 2011[7]
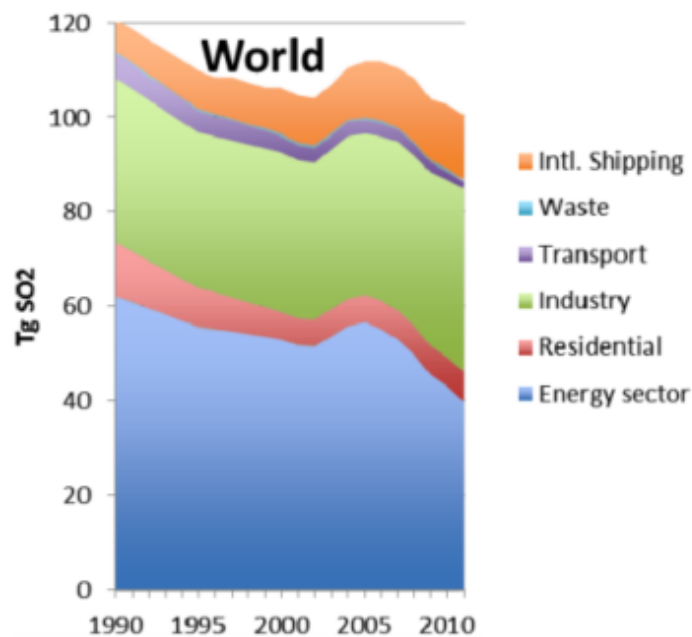
Figure 2.3.1: Sectorial trend in global SO2 emissions since 1990, Tg SO2.

2.4 Nitrogen Oxides

NO_x is an umbrella term to describe nitrogen oxides, primarily NO and NO_2. Nitric oxide (NO) is colorless and odorless while nitrogen dioxide (NO_2) is a orange-brown gas with a distinct pungent odor. These gases can cause damage to the respiratory system by irritating lungs, causing bronchitis and pneumonia, and lower resistance to respiratory infections. In addition to the direct health hazard it poses, NO_x is a contributor to acid rain and a precursor to the formation of ground level ozone, also known as smog[8]. NO_x have been a focus in the automotive industry for a long time, but regulation of NO_x emissions have only recently been implemented in the maritime industry.

In all combustion there are three opportunities for NO_x formation. They are[9]:

1. Thermal NO_x - The concentration of thermal NO_x is controlled by the nitrogen and oxygen molar concentrations, the temperature of combustion and the residence time at high temperatures. Combustion at temperatures well below 1,300°C forms much smaller concentrations of thermal NO_x.

2. Fuel NO_x - Fuels that contain nitrogen create fuel NO_x that results from oxidation of the already-ionized nitrogen in the fuel.

3. Prompt NO_x - Prompt NO_x is formed from molecular nitrogen in the air combining with fuel in fuel-rich conditions which exist, to some extent, in all combustion. This nitrogen is subsequently oxidized along with the fuel and becomes NO_x during combustion, like fuel NO_x.

2.5 Emission Regulations

Due to the harmful effects of the emissions stated above, efforts have been made to reduce said emissions. To combat the maritime sector's contribution to these emissions, a number of regulations have been developed by among others the International Maritime Organization (IMO), the Environmental Protection Agency and the European Union. Of the mentioned legislators, only IMO has a global jurisdiction as it is an agency of the United Nations. This makes it the most influential regulatory body when matters of international shipping is concerned.

MARPOL 73/78 or "the International Convention for the Prevention of Pollution from Ships, 1973 as modified by the Protocol of 1978" is an international maritime convention developed by the IMO to reduce pollution from international shipping. With its 155 ratifying states representing 99.14% of the worlds tonnage[10] it is one of the most important environmental conventions in international shipping. MARPOL has been revised and new annexes and regulations have been added over the course of the years to adapt to new environmental concerns as they present themselves.

MARPOL Annex VI Prevention of Air Pollution from Ships came into effect in 2005 [11]. It established limits and more stringent standards for sulphur oxide, nitrogen oxide and particulate emissions. The emission-control areas (ECA) were established by this annex. These areas were deemed to be particularly sensitive to local pollution from shipping and therefore more stringent emission regulations were imposed. The ECA's can

be seen in Figure 2.5.1. In 2011 a chapter detailing demands for more energy efficient operation was added in order to reduce greenhouse gas emissions from shipping. This chapter made the Energy Efficiency Design Index (EEDI) mandatory for all new ships. The EEDI is a non-presicriptive performance-based mechanism that leaves the choice of efficiency-improvement measures to the industry as long as the requirement for minimum energy efficiency level per capacity mile is met. For different ship designs, a reduction level of grams of CO_2 per tonne mile is set. For the first phase it was set to 10%, and it will be tightened every five years until it reaches a 30% reduction, from a reference of the average efficiency of ships built between 2000 and 2010, in 2025.[12]

Figure 2.5.1: ECA map

In the subsequent years the regulations have become stricter both within the ECA's and in the world as a whole. The development of sulphur fuel content limit can be seen in Table 2.5.1.

Table 2.5.1: IMO sulphur fuel content regulations

Outside an ECA established to limit SOx and particulate matter emissions	Inside an ECA established to limit SOx and particulate matter emissions
4.50% m/m prior to 1 January 2012	1.50% m/m prior to 1 July 2010
3.50% m/m on and after 1 January 2012	1.00% m/m on and after 1 July 2010
0.50% m/m on and after 1 January 2020	0.10% m/m on and after 1 January 2015

IMOs NO_x regulations can be seen in Table 2.5.2[8].

Table 2.5.2: IMO NO_x regulations

Tier	Ship construction date on or after	Total weighted cycle emission limit (g/kWh) n = engine's rated speed (rpm)		
		n<130	n =130-1999	n ≥ 2000
I	1 January 2000	17.0	$45n^{-0.2}$	9.8
II	1 January 2011	14.4	$44n^{-0.23}$	7.7
III	1 January 2016	3.4	$9n^{-0.2}$	2.0

2.6 Emission Reduction Measures

In order to comply with the stricter emission regulations, the maritime industry has to change its practices drastically. Today heavy fuel oil (HFO) is by far the most commonly used fuel for commercial actors in the maritime sector. The sulphur content of HFO can be as high as 3.5% (mass) today, but with the new regulations taking effect, operating using HFO without some exhaust gas treatment system will become illegal. Control of environmental impact and reduction of emissions has become a determining factor in corporate strategies and careful evaluation of the framework of legal, social and economic limitations have become a priority when planning the commissioning and operation of assets.[13] There are two strategic approaches for combustion and emission control. One approach focuses on reducing or eliminating the formation of pollutants. This is called primary or preventive emission control. The second strategy of emission reduction is the secondary or end-of-pipe approach. The goal here is to implement technology that removes or otherwise neutralizes the harm potential of emissions in the flue gas after they are created during combustion.

The choice of emission reduction measures vary according to several different parameters such as price, infrastructure and availability. Some emission reduction measures involves a high initial investment while others have an operational cost or loss of efficiency associated with them. But as the actors in the maritime industry, as in any industry, is in the business of making money the decision will almost always ultimately come down to which technique will bring the operation within compliance of regulations at the lowest cost or lowest loss of income.
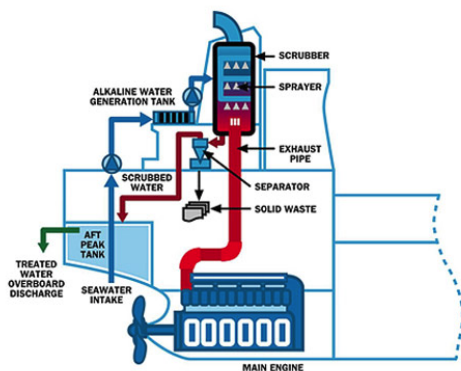
(a) Wet scrubber for SOx and PM removal   **(b)** LNG fueled container carrier concept

Figure 2.6.1: Alternatives for emission reduction

Some methods for emission reduction and their reduction potential were investigated by Elgohary et al.[14]. The results they obtained are shown in Table 2.6.1

Table 2.6.1: Available methods for emission reduction

Component	Reduction method	Potential reduction
CO_2	Energy management	1-10%
PM	Electrostatic filters	<85%
SO_X	Seawater scrubbing; exhaust below waterline	<95%
NO_X	Selective catalytic reduction (SCR)	95%
	Emulsification	20-25%
	Humid air	70\70
	Engine tuning	50-60%
	Exhaust gas recirculation (EGR)	10-30%

2.6.1 Alternative Fuels

Another approach to reducing harmful emissions is to use alternative fuels which produce fewer and less harmful components when combusted. The chemical composition of the fuel is one of the most crucial factors determining both the engine performance and the emission profile. Factors such as sulphur content and carbon-hydrogen ratio are directly linked to the emissions of SO_x an CO_2.

In recent years several alternative fuels have been proposed and tested, each providing strengths and weaknesses both in terms of emissions, performance, price and availability. A qualitative comparison of some of the different alternative fuels was conducted by Banawan et al.[15] The result can be seen in Table 2.6.2.

Table 2.6.2: Qualitative weighting matrix of alternative marine fuels

	NG	Biodiesel	Hydrogen	Alcohol	Bioliquid fuel
Availability	Very good	Very good	Excellent	Very good	Excellent
Renewability	Fairly good	Good	Excellent	Very good	Good
Safety	Excellent	Excellent	Fairly good	Very good	Excellent
Cost	Excellent	Good	Fairly good	Good	Very good
Adaptability	Excellent	Excellent	Good	Good	Very good
Performance	Excellent	Very good	Good	Good	Very good
IMO compliance	Excellent	Good	Excellent	Good	Very good

The comparison revealed LNG as the best alternative for marine application due to reasonably low cost, increasing availability and acceptable adaptabilty to existing engines, with the largest drawback being lack of renewability.

A study conducted by MAN Engines concluded that the use of LNG as fuel for container vessels would promise a low emission profile and, given the right circumstances, lower fuel costs than operation with HFO and a scrubber system. The benefit of using LNG compared to operating on HFO with a scrubber would mostly be dependent on investment costs for the LNG tank system, fuel price difference between LNG and HFO and the percentage of operation being conducted within an ECA. When assuming an equal price increase for LNG and HFO the LNG concept showed to have a shorter payback time

than the ship operating with HFO and a scrubber for all size ranges and proportion of operations spent within ECAs.[16] The LNG price is, however hard to accurately predict due to fluctuations and large local price differences.

The same sentiments are echoed in the second edition of DNV-GL's LNG Report where it is stated that: "LNG as fuel is now a proven and available solution, with gas engines covering a broad range of power outputs"[17]. Additionally it is stated that LNG offers clear environmental benefits in the form of elimination of SO_x emissions, significant reduction in NO_x and PM emissions as well as a reduction in GHG emissions.

With studies indicating the economical viability of LNG as primary fuel and regulatory bodies imposing new restrictions on emissions, the industry now has economical, legal and ethical motivation to innovate and change their practises. These factors, along with developments in storage technology and infrastructure, make LNG the most promising alternative fuel to be considered a large scale replacement for HFO in the years to come.

Chapter 3

Natural Gas Engine Technology

Natural gas has been used to fuel ships for nearly two decades (as of June 2018). The first being the passenger ferry MF Glutra entering into operation in the year 2000. Since then the LNG-fuelled ships in operation and the number of such ships on order have steadily increased. The total number of LNG-fuelled ships, that are not LNG carriers, in operation and on order surpassed 200 in March 2017. Predictions show that the number of non-LNG carrier vessels running on LNG will surpass 1000 within the year 2020 [17]. This trend in the industry shows the need to develop good solutions and optimal engine concepts for operating with LNG as primary energy source.

Figure 3.0.1: The world's first natural gas fuelled ship: MF Glutra

The auto ignition point of methane gas is around 600°C[18]. These kinds of temperatures are unobtainable by compression alone, so using pure natural gas as fuel in a diesel-cycle engine is impossible. However, a number of other engine concepts allow for the use of natural gas as the primary energy source. As of December 2016 there are approximately 120 LNG-fuelled ships in operation. 40% of whom are lean-burn spark ignition (LBSI) engines while the remaining 60% are low-pressure dual-fuel (LPDF) engines [19]. A newer and not as widespread concept is the high-pressure dual-fuel (HPDF) engine. What follows is a brief explanation of the different engine concepts with their advantages and disadvantages.

3.1 Lean-Burn Spark Ignition

The LBSI gas engine operates on the Otto cycle concept and has high excess air, with a fuel-air equivalence ratio (Eq. 3.1.1) of approximately 2. High levels of air excess prevents the spark plug from being operable. The spark plug is therefore placed in a prechamber enriched with fuel gas in order to maintain good operation conditions.

$$\phi = \frac{\frac{m_{fuel}}{m_{ox}}}{\left(\frac{m_{fuel}}{m_{ox}}\right)_{st}} \tag{3.1.1}$$

The lean operation profile of the LBSI engine results in a relatively low combustion temperature which reduces the thermal load on components in the combustion chamber and almost completely eliminates the production of thermal NO_x. This has made the LBSI engine a favored concept along the Norwegian shoreline where there is a NO_x tax. The drawback of this is quenching in the colder parts of the combustion chamber. This makes the combustion incomplete, resulting in an increase in the emission of CO and unburnt hydrocarbons, so-called methane slip. Even though the CO_2 emissions are significantly lowered compared to traditional operations, methane is a potent greenhouse gas with a global warming potential (GWP) of 28[3]. The GWP of 28 implies that each tonne of methane will absorb the same amount of energy as 28 tonnes of CO_2 over a 100 years. The methane slip can therefore cancel out the positive effect of reduced CO_2 emissions. Another disadvantage of the LBSI is that it is sensitive to fuel qualtiy and it lacks the possibility to run on diesel oil if LNG is not available, which explains the shipping industry's preference for dual fuel engines.[19].
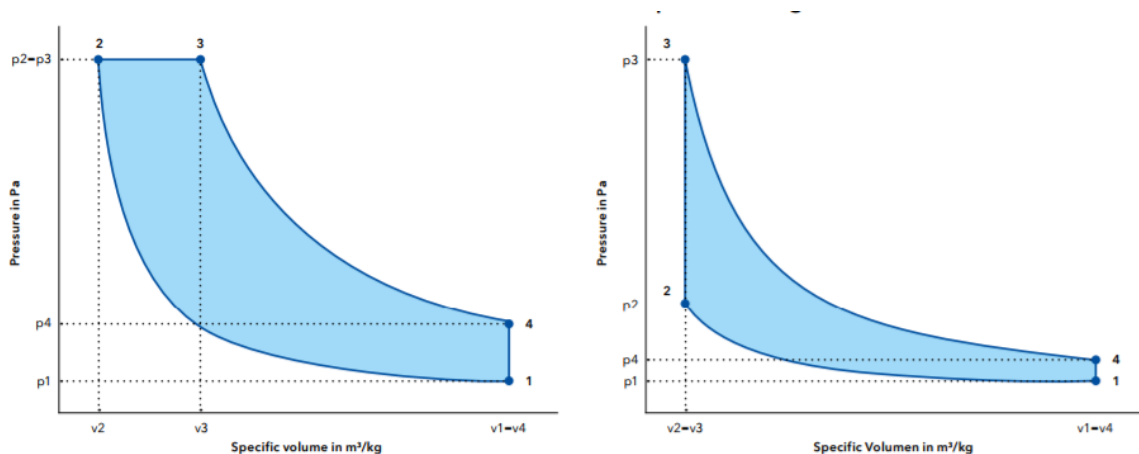
Figure 3.1.1: Diesel and Otto Cycles: pressure-volume diagram. Constant pressure combustion for Diesel and constant volume combustion for Otto

3.2 Low-Pressure Dual-Fuel

The low pressure-dual fuel-engine (LPDF) is similar to the LBSI when it comes to the gas-air mixture. It too operates on a lean premixed fuel/air mixture. When it comes to ignition mechanism, however, it differs. Compression, instead of a spark plug, is used as the ignition mechanism. Thus the LPDF is a compromise between the Diesel and Otto

cycle.

The LPDF engine has the ability to use diesel as backup and therefore holds an advantage over LBSI in that regard. NO_x emissions are in the same range as for LBSI, but can increase if more pilot fuel is used. Therefore the use of pilot fuel contribution is to be as small as possible. Methane slip occurs in the same range as for LBSI at high loads, but higher at low loads due to quenching. This is less of a problem in the 2-stroke LPDF engine than in the 4-stroke models. Another problem with this concept is knocking and pre-ignition if gas fuel of low quality is used.

3.3   High-Pressure Dual-Fuel

The high-pressure dual-fuel (HPDF) engine operates solely on the Diesel cycle concept. Pure air is compressed and pilot fuel and a high-pressure (approximately 350 bar) gas jet is injected directly into the combustion chamber. Compression caused by the piston elevates the pressure and temperature until the pilot fuel ignites, which in turn ignites the gas fuel.

This cycle offers two distinct advantages over the other gas engine concepts. The GHG emissions are significantly lower as methane slip is eliminated. The HPDF is insensitive to fuel quality which makes it more versatile. This concept is also much better suited for conversion of existing diesel engines as it does not need a premixing chamber. The only changes needed for the conversion is a new cylinder head, injection system for the gas and a control system. The drawback is the increased formation of NO_x compared to the lean burn counterparts. The exhaust will have to be treated in order to comply with IMO Tier III NO_x regulations. exhaust gas recirculation (EGR) or selective catalytic reduction (SCR) can be implemented to mitigate these emissions. It is however worth mentioning that HPDF engines still produce 20-30% less NO_x than marine gas oil operation [19]. Another disadvantage is the complexity of the high pressure LNG fuel system. Cryogenic high pressure pumps exist, but are not developed for continuous operation.

In Table 3.3.1, the potential emission reductions of the different natural gas engine concepts are presented. Table data was gathered from SINTEF Ocean's report: "GHG and NO_x emissions from gas fuelled engines"[19].

Table 3.3.1: Potential emission reduction with natural gas operation, for alternative gas engine concepts. Emission reduction in % compared to MGO-operation. No after treatment of exhaust.

Reduction factors compared to MGO	LBSI	LPDF*, 4-stroke Medium speed	LPDF, 2-stroke Slow speed	HPDF, 4-stroke, medium speed	HPDF, 2-stroke, slow speed
CO_2	25-28%	20-25%	20-26%	20-24%	20-24%
NO_x	85-90%	75-90%	75-90%	25-30%	20-30%
SO_x	>99%	98-99%	95-99%	95-97%**	95-97% **
Particulates	>99%	95-98%	95-98%	30-40%	N/A

*)Highest reduction factors for DF obtained with micro pilot ignition
**)Dependent of S-content in pilot fuel

While the HPDF engine seems to be a promising engine concept in the future of the maritime industry, the fact that it operates with high pressure and two separate fuels, both needing an individual injector, makes it a far more complex engine than conventional diesel engines. Factors such as injection pressure, temperature and timing as well as injector positions all play a vital role in the operation and performance of the engine. Therefore, determining precise specifications and operation profile of the fuel injectors and is an absolute necessity .

Chapter 4

Important Characteristics

4.1   Gas Jet Characteristics

In direct injection engines there is short time for mixing to occur. Therefore an understanding of the characteristics of the gas jet is crucial in order to facilitate good combustion conditions.

4.1.1   Penetration Length and Cone Angle

Accurate determination of macroscopic characteristics such as the jet tip penetration, speed and angle for representative pressure ratios can be used to design better injection schemes, and is therefore very valuable. Larger penetration and jet cone angle can increase the jet volume and with this also increase air utilization, while a short jet tip penetration might be necessary if wall impingement has to be avoided[20].

The following model for determining jet tip penetration length was derived by Hill and Oulette [21]:

$$S_t = \Gamma (d_n U_n)^{\frac{1}{2}} \left(\frac{\pi}{4} \frac{\rho_n}{\rho_\infty}\right)^{\frac{1}{4}} t^{\frac{1}{2}} \tag{4.1.1}$$

Where U_n is the jet velocity at the nozzle, d_n is the nozzle diameter, t is time, ρ_n is the gas density at the nozzle and ρ_∞ is the chamber gas density. Γ is the penetration constant and is equal to 3 ± 0.1. [21]

The jet tip penetration is characterized as the distance from the injector nozzle to the front edge of the gas jet. The cone angle is defined as the angle at which two lines from the extreme values of the spray in radial direction intersect.
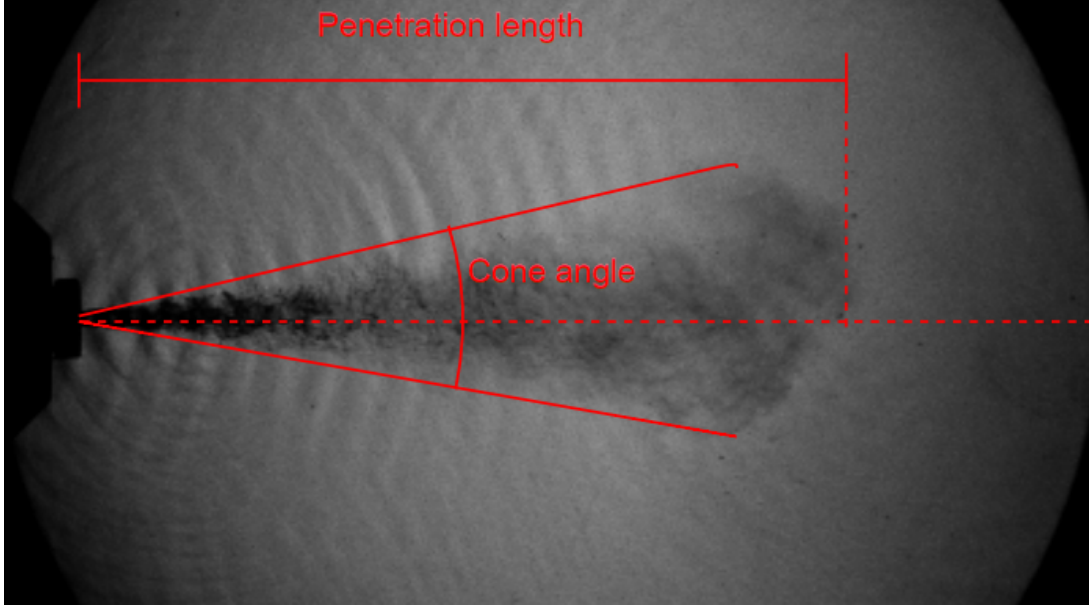
Figure 4.1.1: Gas jet penetration length and cone angles definition

If these parameters are known and an assumption is made that the jet is axi-symmetrical the jet volume can also be determined. As this study implemented nozzles that were not axi-symmetrical in addition to the circular nozzles, this assumption could not be made and thus no effort was made to determine the volume of the jet.

4.1.2 Choking and Sonic Velocity

Choking of a flow is an important phenomenon when it comes to the study of fluid dynamics. In engineering valves and calibrated nozzles can produce a specific mass flow rate independent of downstream conditions, when the flow is choked. When a flow is choked, lowering the downstream pressure while keeping the upstream pressure fixed will not increase the mass flow. Increasing the upstream pressure can, however, increase the flow as velocity is the limiting factor and increased upstream pressure will increase the fluid density[22]. For homogeneous fluids the choking phenomenon will occur at the local sonic velocity, Mach 1 [23]. Sonic velocity, a, is given as:

$$a = \sqrt{\kappa R T} \tag{4.1.2}$$

Where κ is the ratio of specific heats, R is the gas constant and T is the local absolute temperature.

4.1.3 Shock Structure

A high injection pressure and a converging nozzle leads to an under-expanded gas jet at the nozzle exit, meaning the gas jet leaves the nozzle at a pressure higher than ambient pressure. The shock wave structure near the jet affects the injection and mixing properties of the jet. The gas is decelerated from supersonic to subsonic velocity as it passes through a normal shock known as the Mach disk[24]. An increased Mach disk width leads to a large jet near-field angle which promotes the spatial distribution and turbulent mixing of gas jet [25]. A visual explanation of the near-nozzle gas jet shock structure can be seen in Figure 4.1.3.
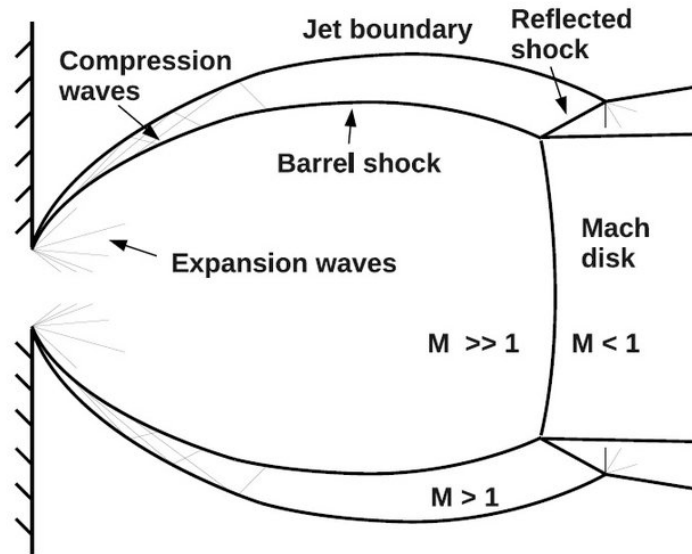
Figure 4.1.2: Shock structures forming the Mach disk in an under-expanded supersonic free jet
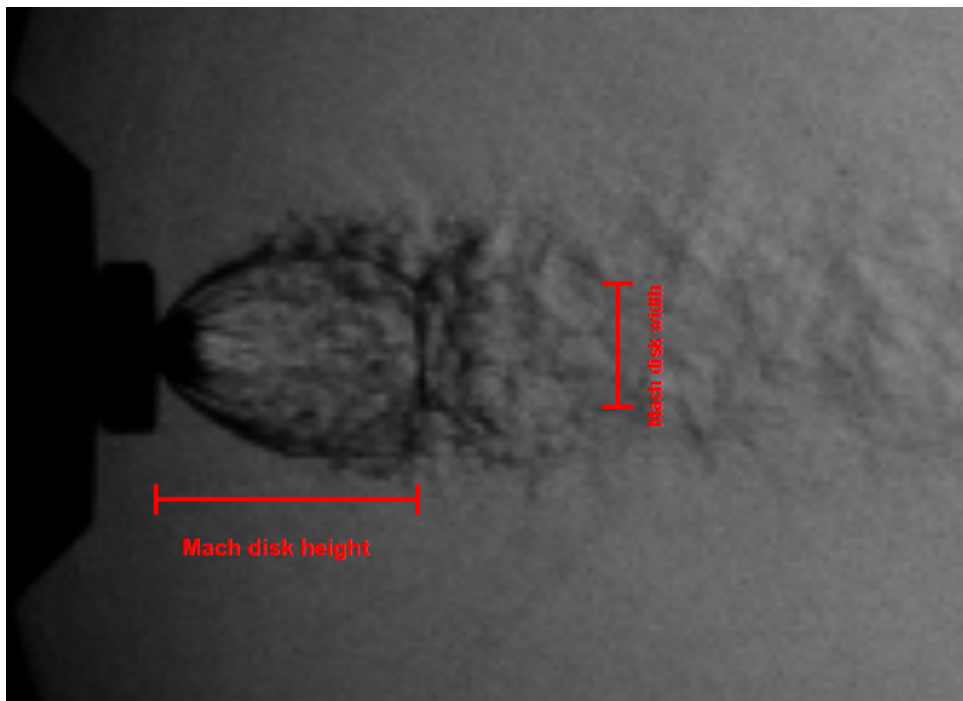
Figure 4.1.3: Schlieren image of shock structure, Inj.Pressure:381bar, Ch.Pressure:1bar

Ashkenas and Sherman studied the relationship between mach disk height, nozzle diameter and nozzle pressure ratio (NPR) and came up with the following relation[26].

$$\frac{H}{d_n} = 0.67\sqrt{\frac{P_i}{P_b}} \tag{4.1.3}$$

Where d_n is nozzle diameter, H is Mach disk height, P_i is injection pressure and P_b is ambient pressure.

4.2 Injector Characteristics

The jet characteristics are not only dependent on the strictly fluid properties such as the pressure ratios, but they are also highly dependent on the geometrical characteristics of the injector.

4.2.1 Discharge Coefficient

When calculating theoretical values for flows one often operates under the assumption of isentropic conditions. The actual flow through a control volume is never isentropic, due to frictional and contraction losses in the fluid jet. The discharge coefficient C_D is the ratio of actual discharge to the theoretical discharge through a constriction[27]. Precisely determining the discharge coefficient is essential, as errors in the discharge coefficient will inhibit future calculations of mass flow even if other parameters are accurately determined [28]. Accurately determining the mass flow of your injector is a prerequisite for knowing the energy supplied to your system in the form of fuel. This is especially relevant for a dual-fuel concept that might have several different operation modes where the percentage of energy delivered to the combustion chamber provided by the gas injector might vary drastically.

To calculate the discharge coefficient the following formula was used: [29]

$$C_D = \frac{\dot{m}\sqrt{RT}}{AP_u\sqrt{\frac{2\kappa}{\kappa-1}\left(\frac{P_d}{P_u}^{\frac{2}{\kappa}} - \frac{P_d}{P_u}^{\frac{\kappa+1}{\kappa}}\right)}} \tag{4.2.1}$$

Where $\dot{m}$ is the mass flow rate, R is the gas constant, T is the gas temperature, Pu is the upstream injection pressure, Pd is the downstream pressure(in this case ambient pressure), κ is the specific heat ratio and A is the smallest flow area in the flow's path, the throat area.

When the pressure ratio falls below the critical value

$$\frac{P_d}{P_u} = \left(\frac{2}{\kappa+1}\right)^{\frac{\kappa}{\kappa-1}} \tag{4.2.2}$$

sonic conditions will occur in the throat of the injector and the flow is choked. For nitrogen gas this downstream-upstream NPR will be approximately 0.53, but it will vary somewhat as the specific heat capacities are pressure and temperature-dependent. When the pressure ratio passes the critical value, $\frac{P_d}{P_u}$ will be replaced with the critical value and we obtain the following expression for the choked flow discharge coefficient

$$C_D = \frac{\dot{m}\sqrt{RT}}{AP_u\sqrt{\kappa\frac{2}{\kappa+1}^{\frac{\kappa+1}{\kappa-1}}}} \tag{4.2.3}$$

4.2.2 Injector Throat Area

Knowing the throat area, or the smallest flow area, of the injector at all times was critical for determining the discharge coefficient. From the conservation of mass equation,

Eq.(4.2.4), it can derived that the highest velocity occurs at the throat and this is where the choking will take place.

$$\dot{m} = \rho V A \tag{4.2.4}$$

V is the gas flow velocity.

From the injector specifications it could be seen that the throat area would either be the nozzle area or the area created by lifting the blocking needle. A sketch showing the injector nozzle and needle can be seen in Figure 4.2.1
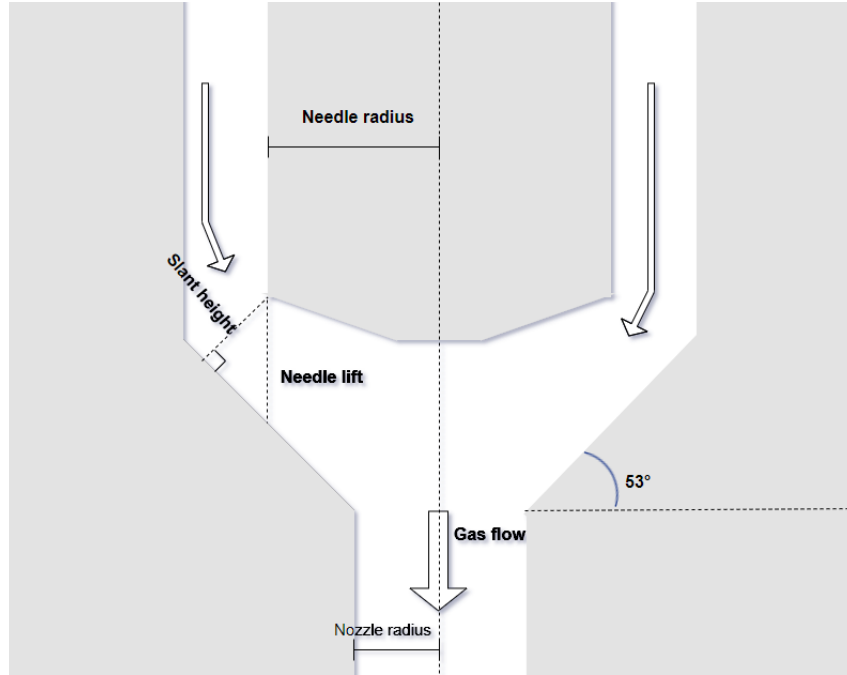
Figure 4.2.1: Cross section sketch of injector tip with needle. (Not to scale)

The flow area created by the needle's lift takes the form of the surface area of a truncated cone with slant height as seen in Figure 4.2.1. The lateral surface area of a truncated cone is:

$$A_{surface} = \pi(r_{inner} + r_{outer})s \tag{4.2.5}$$

Where s is slant height. By using data from the CAD-drawings of the injector and inputting it in the equation above, an expression was derived for the flow area as a function of the needle lift.

$$A_{flow} = \frac{\pi}{1.705}l(2r_{needle} + 0.48l) \tag{4.2.6}$$

Where l is needle lift. The resulting throat area is then:

$$A = min(\pi r_{nozzle}^2, \frac{\pi}{1.705}l(2r_{needle} + 0.48l) \tag{4.2.7}$$

Figure4.2.2 shows the increase in flow area as the needle is lifted. The constant lines represent the nozzle areas for the different nozzles used in this study.

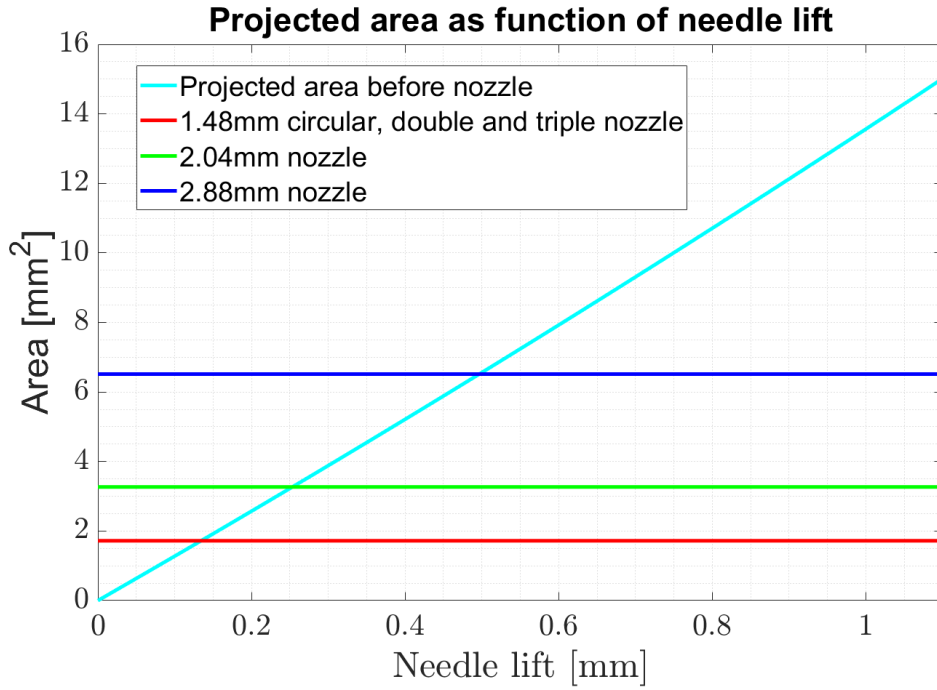**Figure 4.2.2:** Flow area

The exact needle lifts that produce an internal flow area equal to the nozzle area are shown in Table 4.2.1.

Table 4.2.1: Needle lift to produce equal area

Nozzle diameter[mm]	Nozzle area[mm^2]	Needle lift [mm]
1.48	1.720	0.134
2.04	3.269	0.253
2.88	6.514	0.497

Chapter 5

Imaging Techniques

In order to assess the characteristics of the injected fluid, an optical analysis was conducted. Optical analysis processes are beneficial as they are non-intrusive and have high temporal and spatial resolution. It is excellent for obtaining qualitative data, but quantitative data may be difficult to gain from such an analysis. The equipment needed to perform an analysis of satisfactory quality in this manner is also rather expensive. The main types of optical probing systems are shadowgraphs, schlieren and interferograms, each displaying their distinct set of intrinsic merits and limitations.[30] For the experiments performed in this thesis, schlieren and background-oriented schlieren was utilized.

5.1   Schlieren

Schlieren photography is used to visually depict inhomogenities in transparent media that are not otherwise visible to the naked eye. The word "schlieren" is a German word meaning "streak". The principle has been used for several centuries by early astronomers and glass-makers to detect irregularities in glass and optics. The working principle of Schlieren photography is the change in refractive indices as the density changes. For air and other gases this relation is linear and can simply be expressed as seen in Eq.(5.1.1) [31]

$$n - 1 = k\rho \tag{5.1.1}$$

where k is the Gladstone-Dale coefficient, n is the refractive index and ρ is the fluid density.

$$\frac{P}{\rho} = RT \tag{5.1.2}$$

Assuming that the gas behaves according to the ideal gas law and by combining Eq.(5.1.1) and Eq.(5.1.2) it can be seen that the brightening and darkening caused by the streaks (schliere) in the image will represent changes in composition, pressure and temperature.
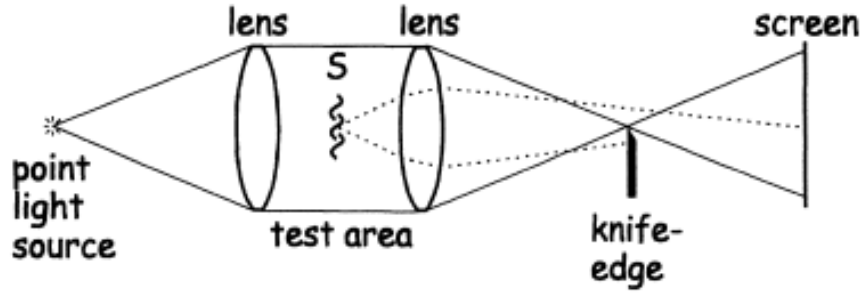
Figure 5.1.1: Schlieren concept sketch

The basic concept of a Schlieren imaging setup can be seen in Figure 5.1.1. A point light source is passed through a lens, the test area and then through another lens that re-focuses the light. The inhomogenities in the test area will deflect some of the light beams. A sharp edge (often a razor) is placed in the focal point of the lens in such a way that it blocks the deflected light and part of the undeflected light. This creates an enhanced contrast which will reveal an image of the density gradients perpendicular to the edge orientation. By adjusting the orientation of the edge of the razor one can set the direction of the density gradient field shown in the image. Even radial density gradients are obtainable if a circular edge is used.

A CAD-model of the schlieren setup used in this study is shown in Figure 5.1.2.
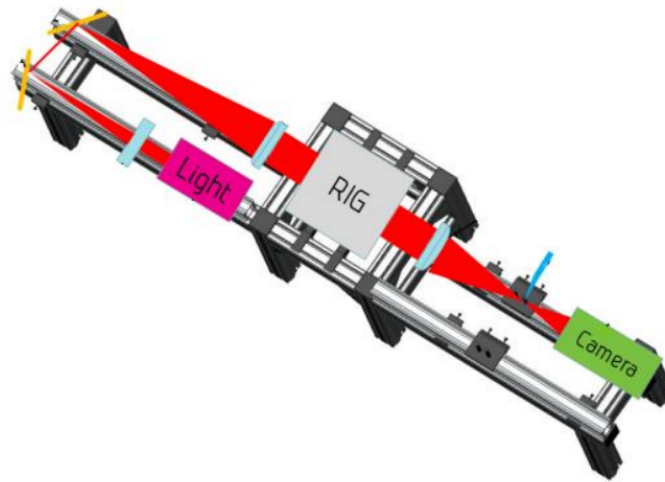
Figure 5.1.2: Schlieren system

5.2 Background-Oriented Schlieren

Conventional schlieren techniques have been used for several decades and are proven to provide excellent qualitative results, but can be lacking when it comes to providing quantitative results. The BOS technique is an optical density visualization technique which is similar to conventional schlieren as it too relies on the refractive index' density dependence to extract data from images. It also shows several similarities with laser speckle

photography as described by Wernekinck and Merzkirch. [32]

In addition to qualitative results the BOS method has the potential to yield qualitative results, the most important of which is the determination of density fields by integration of the measured gradient fields.[33] Knowing the density distribution and having an accurate estimate of the density field can be incredibly valuable information when studying gas jet dynamics. With an accurate representation of the density field, huge leaps can be made in optimizing the injector and chamber design, and the injection process in order to get better mixing conditions and in turn more favorable combustion conditions.

Figure 5.2.1: BOS concept sketch

Compared to other optical speckle pattern techniques, BOS simplifies the experimental process and reduces the requirement for expensive 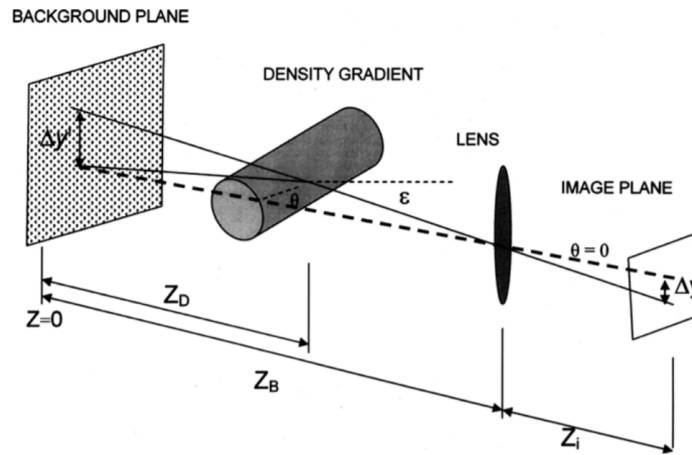equipment. The light source is directed through a transparent sheet with a speckle pattern consisting of small randomly distributed dots. It is important that the spacial frequency of the dots is high enough to be imaged with high contrast. Further, the light beam travels through the test field with a density gradient which results in a deflection. The light is then passed through a lens before it is captured by the camera at the image plane.

Assuming paraxial recording and small deflection angles ($\varepsilon \approx \tan \varepsilon$), the image displacement of each dot is given as:

$$\Delta y = f \left(\frac{Z_D}{Z_D + Z_A - f} \right) \varepsilon \tag{5.2.1}$$

Definitions of distances Z_D, Z_A and Δy as well as angle ε can be seen in Figure 5.2.1. f is the focal length of the lens.

The procedure of a BOS recording and analysis is usually performed as follows: First a reference image of the undisturbed background pattern has to be captured. The second step is to record the flow under investigation, for this study during gas injection. This leads to a locally displaced image of the background pattern, a virtual displacement of the dots, due to density difference. The images of the flow can then be compared to the reference frame and evaluated by image correlation methods. Already existing methods optimized for particle-image velocimetry (PIV) or other forms of speckle photography can

be used to determine the background image displacement without further effort.[34]. The deflection of each light ray holds information about the spatial gradient of the refractive index integrated along the line of sight as can be seen in Figure 5.2.1

Beneath is a pair of images comparing the disturbed and undisturbed cases.

(a) Undisturbed image   (b) Image disturbed by gas jet
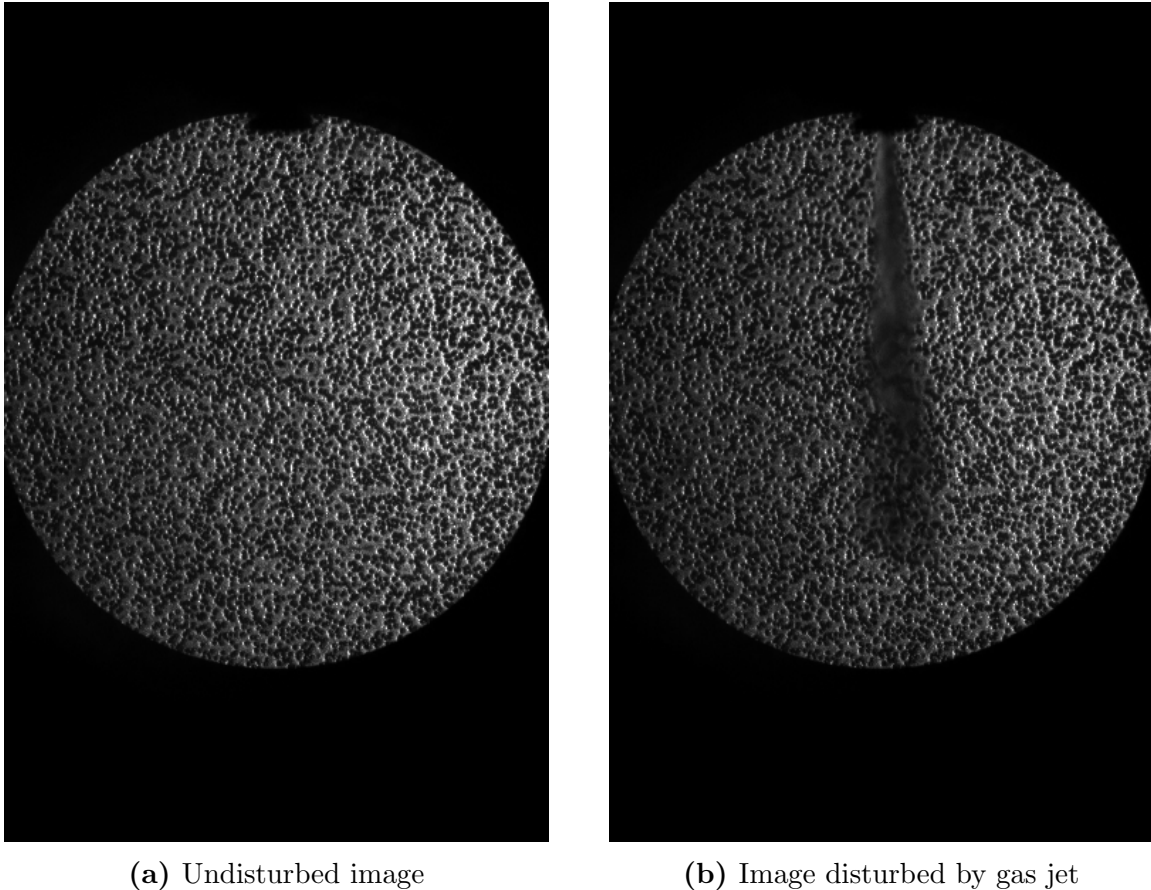
Figure 5.2.2: BOS photos before and during injection

The BOS technique relies heavily on the use of numerical methods in order to convert the information in the displacement field to the corresponding density field. It is generally possible to use a finite difference approximation or a Poisson solver to integrate the density gradient field to determine the relative density field in the flow. If the absolute density is known somewhere in the observation, this can be used to determine the density in all points in the flow. However, any non-twodimensionality in the flow field can distort the results, since the BOS method is a line-of-sight integrating technique[35].

Chapter 6

Research Equipment

6.1 Constant Volume Combustion Chamber

To conduct the optical injection analysis, injections were directed into a constant volume combustion chamber (CVCC) with a volume of 6.8 liters. The CVCC has no moving parts, thus enabling the isolation of the injection and combustion process from any influence of piston movement or other disturbances. No combustion tests were conducted in this study. The ambient pressure in the chamber where the gas is injected is one of the most influential parameters for the injection characteristics. The chamber is equipped with two windows for optical access which makes it possible to capture the fluid interactions with a high speed camera.
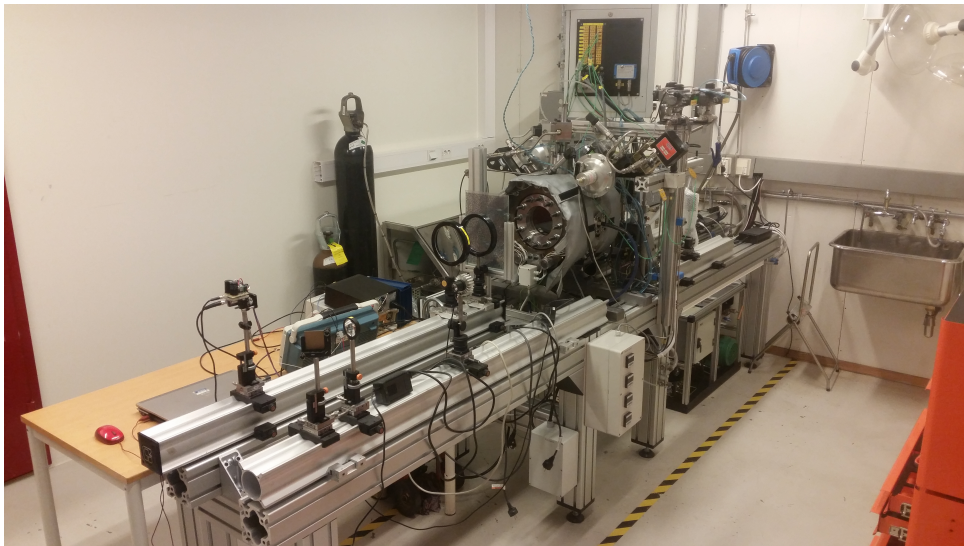
Figure 6.1.1: Photo of the experimental setup

6.2 Gas Injector

Gas was supplied to the system using a prototype single-nozzle gas injector capable of delivering gas at high pressures comparable to those found in high pressure dual fuel engines. The injector nozzle is blocked by a needle preventing the gas from escaping and when this needle is lifted the gas is allowed to flow out of the nozzle. The injector-nozzle

is interchangeable, enabling testing with different nozzle diameters and geometries. In the experiments performed, three circular conical nozzles with diameters of 1.48mm, 2.04mm and 2.88mm and two non-circular nozzles were used. The non-circular nozzles had the same area as the circular nozzle with 1.48mm diameter. The shape of these nozzles can be seen in Figure 6.2.2 and will from now on be referred to as the double- and triple nozzle.
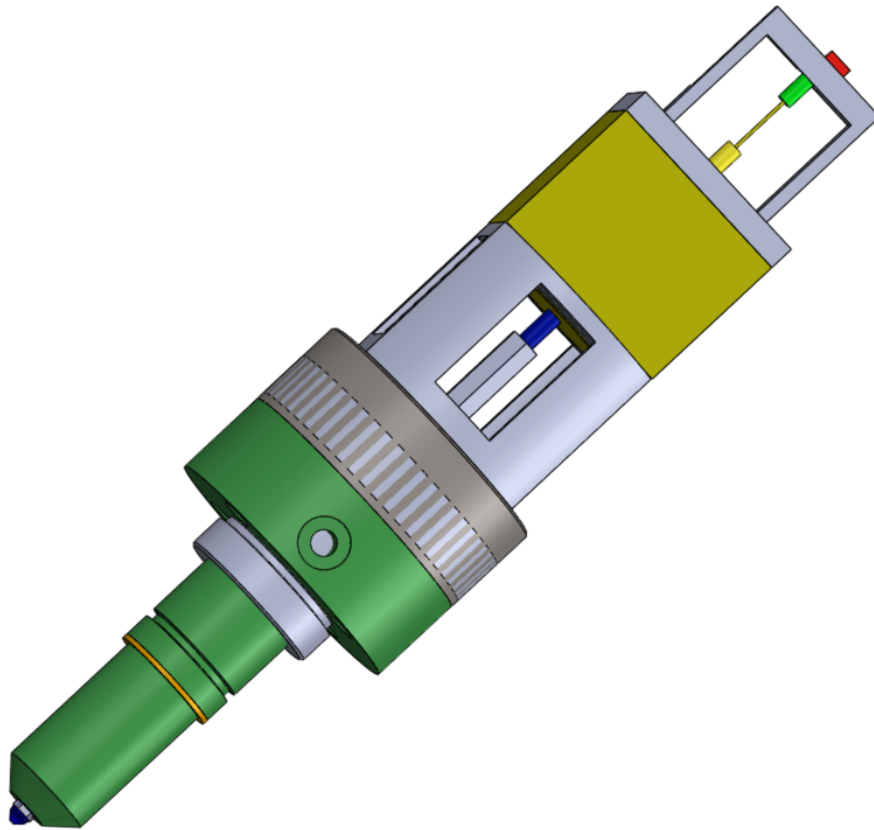
Figure 6.2.1: 3D CAD model of gas injector

(a) Circular nozzle   **(b)** Double nozzle   **(c)** Triple nozzle
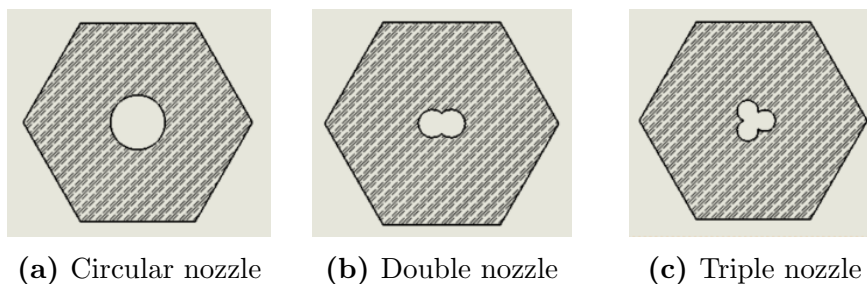
Figure 6.2.2: The nozzle geometries used in this study

More details on the injector and its constituent parts can be seen in Appendix A and Appendix B.

6.3 Sensors and Measurement Equipment

In order to determine the operation profile of the equipment, relevant quantities had to be measured and logged. The following types of sensors were used:

6.3.1 Thermocouple

Thermocouples consist of two dissimilar electrical conductors which form electrical junctions at different temperatures. The thermoelectric effect is utilized to produce a temperature-dependent voltage which can be logged in order to determine the temperature at a certain point in the flow.

A wide measurement range and inexpensive and interchangable parts make the thermocouple a popular sensor for research and industrial applications. The main limitation of the thermocouple is its inaccuracy. Determining temperatures with error less than one °C is challenging. Another disadvantage is that it is an intrusive measurement device that can disturb the flow around the sampling point. These factors were not issues for the research conducted in this study.

6.3.2 Pressure Sensor

To measure the gas flow pressure right before the injector a GE UNIK 5000 industrial accuracy pressure sensor with range 0-700 bar was used.

6.3.3 Flowmeter

To measure the mass flow through the injector a flow meter of the type SITRANS F C MASS 6000 was used. This flowmeter was used for its fast flow step response and high flow capacity. The accuracy of the measurements were, however, limited when the duration of the injections were short.

6.3.4 Needle-Lift Sensor

The needle lift was measured by combining a Hall effect sensor mounted at the stationary back end of the injector with a magnet fastened to the rear of the needle. The Hall effect sensor is a transducer that will vary its output voltage in response to a magnetic field[36]. A thin metal strip is subjected to a current along it and the presence of a magnetic field will cause some of the electrons to be deflected towards one side of the edges. This will induce a voltage gradient across the strip perpendicular to the feed current. As the needle is lifted, the magnetic field across the sensor changes. The sensor registers this change and generates a voltage response, which in turn can be translated to a corresponding relative position.

This sensor, which is widely used in industrial applications for its accuracy and high sampling rate, was chosen to achieve an accurate reading of the needle movement.

6.4　Chamber Gas Supply

The CVCC is equipped with a system of gas containers enabling it to pressurize and produce different mixes of gases in the chamber. In the tests conducted in this thesis air was the chosen ambient gas in the chamber. Additional nitrogen was pumped into the chamber when higher pressure was desired.

6.5　Gas Compression System

To achieve higher injection pressures than the one supplied from the 200bar gas bottles, a compressor from Proserv was used. This compressor uses an air-driven Haskel pneumatic booster pump that utilizes pressurized air to compress the working medium to required pressure.

6.6　The Working Medium

For all the tests conducted during this study, nitrogen gas was used as the working medium. Initially natural gas, hydrogen and mixtures of the two were intended to be used, but because of a small leak in the injector this was not deemed safe. Nitrogen is a non-reactive and non-toxic gas which ensured that the testing would not pose any breach of HSE procedure. In addition to the HSE aspect, nitrogen was used because it is substantially less costly than the other gas mixes and a large number of tests were to be conducted. Ideally a gas mixture representative of what could be found in a HPDF-engine would have been used. Nitrogen was deemed an acceptable substitute, given that the objectives of this study largely revolved around investigating effects dependent on nozzle geometry and pressures. The nitrogen was supplied from 50l gas bottles with a maximum pressure of 200bar

6.7　Hydraulic Servo Valve

To lift the needle and open the injector, a hydraulic servo valve from MOOG was used. Servovalves are electrohydraulic valves that transform an analog or digital input signal into a stepless hydraulic output. This kind of actuator suffers from slow response when compared to, for example, a solenoid valve.

6.8　Regulator

A Messer EN ISO 2503 cylinder pressure regulator was used to regulate injection pressure for the out-of-rig tests. The regulator allowed for testing at different injection pressures and provided the ability to perform several tests with the same injection pressure, even as the gas bottle emptied and lost some of its pressure. It also limited the amount of gas spent on each injection, so more tests could be conducted without exhausting the gas

supply.

6.9   High-Speed Camera

The high-speed camera used for the optical analysis performed was a Photron Fastcam SA-X2. This camera had high enough frame rate (temporal resolution) and display resolution to provide a satisfactory basis for analysis.

6.10   Light Sources

For the two different optical setups two different light sources were used. The BOS-analysis was conducted using a green photo-electric pulsating diode. For the conventional Schlieren tests a white light-emitting diode (LED) with constant light output served as the light source.

6.11   Control and Logging System

A custom made interface in LABview was used to control the system. The settings of the injection process was determined by choosing the needle uptime, downtime and number of pulses in a sequence. The output from all of the sensors were fed back into the computer and stored as a .txt file. The data could also be displayed as graphs in the LABview interface.

Chapter 7

Test and Analysis Procedures

There were two primary test scenarios for the experiments conducted during the work associated with this thesis. One set of experiments were performed without mounting the injector in the rig. The intent of these tests was to quantitatively determine gas injection operation and the internal losses imposed on the flow due to geometrical conditions in the injector.

Some similar experiments were performed while working on the project thesis during the autumn semester of 2017, but it was deemed necessary to establish a more extensive data basis and more stringent testing procedures to obtain more reliable results, which could be used in further testing.

For the other test scenario, the injection was done into the CVCC. These tests were conducted in order to perform an optical analysis to investigate the effect of nozzle geometry, injection pressure and ambient pressure on the gas jet shape and propagation. Two optical analysis methods were used and a total of 200 injections were done into the chamber, 100 for each imaging method.

All tests were performed in SINTEF Ocean's combustion laboratory in Trondheim with ambient conditions being air at 1atm pressure and approx. 20 °C if not otherwise specified. The injected medium was nitrogen for all tests conducted.

7.1 Injector Performance Study - Outside Rig

Every test outside of the rig was performed with a regulator connected to the gas supply. This allowed for multiple tests at the same pressure and it prevented wasting nitrogen as there was no need to inject at maximum pressure for these tests. All sensor data was logged and stored on the control unit. The test system configuration for the testing done outside the rig can be seen in Figure 7.1.1
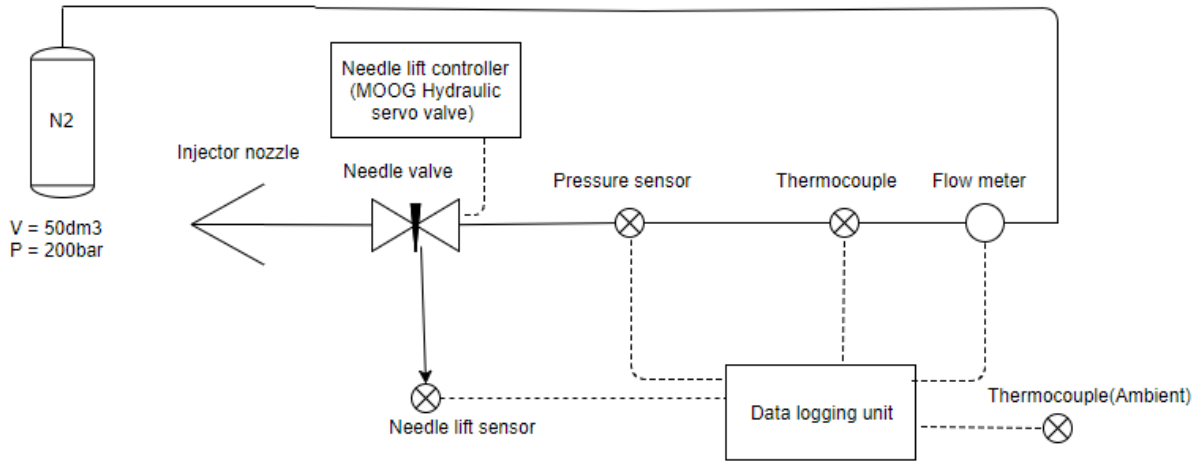
Figure 7.1.1: Test setup for testing outside of the rig

The first series of experiments had steady flow, pressure and temperature conditions. Pulses with a duration of two seconds were able to achieve such conditions. 45 injections with a duration of two seconds at several different pressures were performed to sample steady state conditions for a fully opened injector. Nine shots were done for each nozzle for the steady-state tests.

Due to the fact that the different nozzles resulted in different pressure losses at the same back pressure, the injection pressure was not controllable. However, all of these injections were in the choked region so this was not an issue, as the discharge coefficient will almost be unaffected by pressure ratio in the choked flow region. [37].

The tests with long pulses resulted in substantial pressure drops during the injection and could did not take into account the effect of the changing throat area that occured as the needle lifted. Therefore a number of tests were conducted to investigate the performance of the injector under more dynamic conditions.

30 series of injections were done in short bursts in order to gather data on the injector operation in the transient phase and in order to limit pressure drop. 15 of these were done in series of 60 bursts with 10ms uptime and 20ms downtime, while the remaining 15 tests were series of 30 bursts with 20ms uptime and 40ms downtime.

The last series of tests outside of the rig were single shots with short duration, in the interval of 2-10ms, to determine needle movement for the shortest injection times.

7.2   Optical Study - Injector Mounted In Rig

For the optical tests the shortest possible needle lift signal, 2ms, was chosen. This was due to the fact that the hydraulic servo valve responsible for the needle lift was slow, so the shortest possible needle lift signal would be the one resulting in the most realistic opening time. 750 images were captured for each test. This ensured that the entire injection was

captured from start to finish for all experiments.

For each imaging technique the nitrogen gas was injected at two different injection pressures, approximately 218 bar and approximately 381 bar. Because of difficulties of adjusting the compressor, the actual injection pressures did vary quite substantially, as can be seen in Table 7.2.1. Half of the injections were done into the chamber at atmospheric pressure. For the other half, in order to more closely resemble the density in an engine, nitrogen was pumped into the chamber to increase the pressure to approximately 20bar. This brought the chamber density close to the experimental standard density established by the Engine Combustion Working group of 22.8 kg/m^3[38]. For each combination of injection pressure and chamber pressure, five injections were performed with each nozzle, totalling 100 injections for each imaging technique.

To make sure that all tests were performed according to procedure and to have a record of boundary conditions for later, measurement protocols were created. One measurement protocol was established for each nozzle for each of the two imaging techniques employed in this study. Ten separate measurement protocols with 20 measure points each were created in total, covering all 200 tests in the optical study. An example of one of the measure protocols can be seen in Appendix C.

Table 7.2.1: Injection and chamber pressures and deviations for the optical study

	Mean	Max	Min	Std. Deviation
$P_{inj.low}$[bar]	217.8	230.7	210.0	3.84
$P_{inj.high}$[bar]	381.3	393.8	370.7	4.32
$P_{ch.low}$[bar]	1.2	1.7	1.0	0.22
$P_{ch.high}$[bar]	20.4	21.1	19.2	0.52

It was necessary to know the conversion factor between pixels and mm in the images captured. This was done by placing a ruler in the CVCC and using PFV's built-in distance tool. The conversion factors for the two different optical setups are specified in their respective subsections.

For all of the tests conducted in the optical studies it was made sure that the non-circular nozzles were mounted in the same orientation in relation to the camera for all tests. The double nozzle was aligned perpendicular to the camera and the triple nozzle was aligned in such a fashion that one of the bulges pointed towards the camera. For the circular nozzles this was not an issue as they are symmetrical around every axis.

7.2.1 Background-Oriented Schlieren Study

The intent of the BOS study was to determine the density field of the injected gas jet. The light source used for these tests was the pulsing photo-electric diode, so before each test an oscilloscope was used to synchronize the light pulses and the camera's shutter making sure that lighting was even for each frame captured.

Setting	
Frame Rate [pic/s]	40 000
Shutter Speed [s]	1/400000
Resolution [pxl]	384 x 592
Pixel to mm conversion [pxl/mm]	0.333

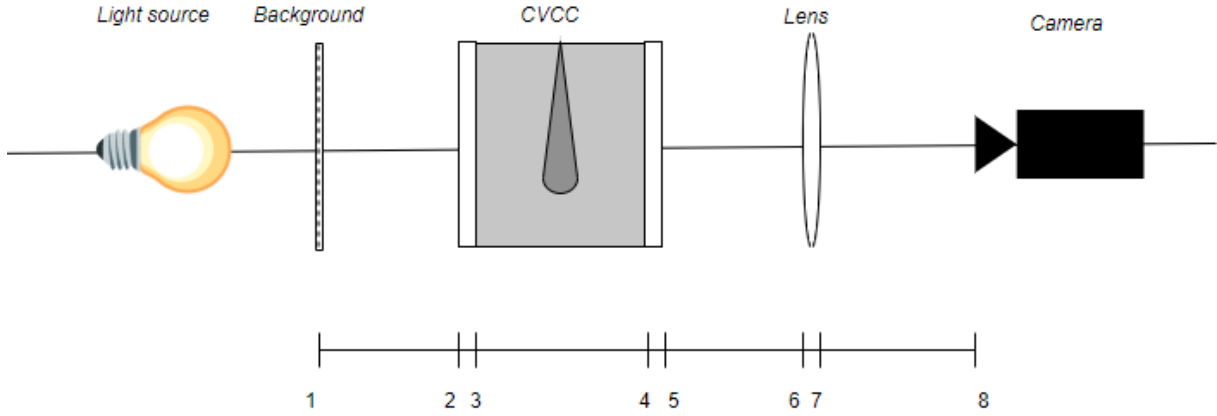The test setup from the BOS tests can be seen in Figure 7.2.1.

Figure 7.2.1: BOS test setup. Important cross-sections are marked 1-8.

After experimenting with several different dot patterns for the background of the BOS setup the following parameters were chosen: The size of each dot was approximately 3.5x3.5 pixels and the dot density was around 0.34 dots/mm2.

Image analysis

For the analysis of the BOS-images, attempts were made to use MATLAB's built-in radon and inverse radon transform. This was done in order to filter the images and account for the 3D nature of the test case, but it did not notably change the resulting density field.

The displacement field was established by using the PIVlab script developed by Dr. William Thielicke.[39] [40]. This script uses fast-fourier transform based cross-correlation to compare the images to the reference and measure the displacement. The interrogation window was set as small as possible, 4x4 pixels with a step of 2 pixels, to obtain the highest possible resolution of the displacement field.

Poisson integration was used to calculate the refractive index at each point from the obtained displacement field. The generic Poisson equation can be seen in Eq.(7.2.1)

$$\nabla^2 u = f(x, y) \tag{7.2.1}$$

For a 2D-case the equation becomes:

$$u_{xx} + u_{yy} = f(x, y) \tag{7.2.2}$$

Every time the light crosses over from one medium to another with a different density, the light will be refracted. In our case this refraction will occur 7 times at air-glass, glass-nitrogen, nitrogen-glass, glass-air, air-lens and lens-air interfaces. Therefore, the contribution of each of the media had to be taken into consideration when the images were to be analyzed in order to reconstruct the density field. [41]. This was done by applying a multiplier, K, to the solving scheme. K is the inverse of the contributions from each layer of a different medium.

$$K = \left[2 \sum_{i=1}^{N} \frac{H_i^2}{n_i}\right]^{-1} \tag{7.2.3}$$

Where H is the thickness of each layer, and n_i is the approximate refractive index of the medium.

Table 7.2.3: Cross section specifications

Section	Medium	Length [mm]	Refractive index
1-2	Air	400	1.0
2-3	Sapphire glass	40	1.8
3-4	Nitrogen	175	1.0
4-5	Sapphire glass	40	1.8
5-6	Air	205	1.0
6-7	Glass (lens)	5	1.5
7-8	Air	200	1.0

The refractive indices in Table 7.2.3 are rounded off to one decimal point. The most important thing was to account for the contribution of the lens and the sapphire glass windows in the rig which had substantially higher refractive indices than the other media.[42]

The following equation describes the applied Poisson for our case:

$$\Delta n = \frac{\partial^2 n}{\partial x^2} + \frac{\partial^2 n}{\partial y^2} = K\left[\frac{\partial}{\partial x}\Delta x + \frac{\partial}{\partial y}\Delta y\right] \tag{7.2.4}$$

where Δx and Δy are the displacements in horizontal and vertical direction respectively.

A MATLAB script using a five point finite difference solving scheme was adapted to solve the discrete Poisson equation. A five point-stencil is made up of one grid point and its four "neighbors" [43]. With this scheme one can write finite difference approximations to derivatives at grid points. The tolerated error of the solver was set to 10^{-3}

$$u_{i+1,j} + u_{i,j+1} + u_{i-1,j} + u_{i,j-1} - 4u_{i,j} = f(x, y) \tag{7.2.5}$$
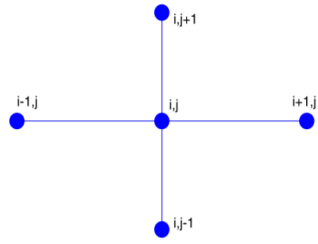
Figure 7.2.2: Five point stencil

In order to solve Eq.(7.2.4) a set of boundary conditions had to be implemented. Dirichlet boundary conditions were set as the maximum and minimum refractive indices possible for the conditions obtainable in the chamber during injection. This was dependent on the injection pressure and chamber pressure. Due to the dynamic nature of the entire volume inside the chamber, there was no way to know the exact refractive index at the edges of the observational window, thus it was hard to implement Neumann type boundary conditions.

When a field of refractive indices had been obtained, the Gladstone-Dale relation was implemented to find the corresponding densities.

The entire process of the BOS procedure can be seen in Figure7.2.3
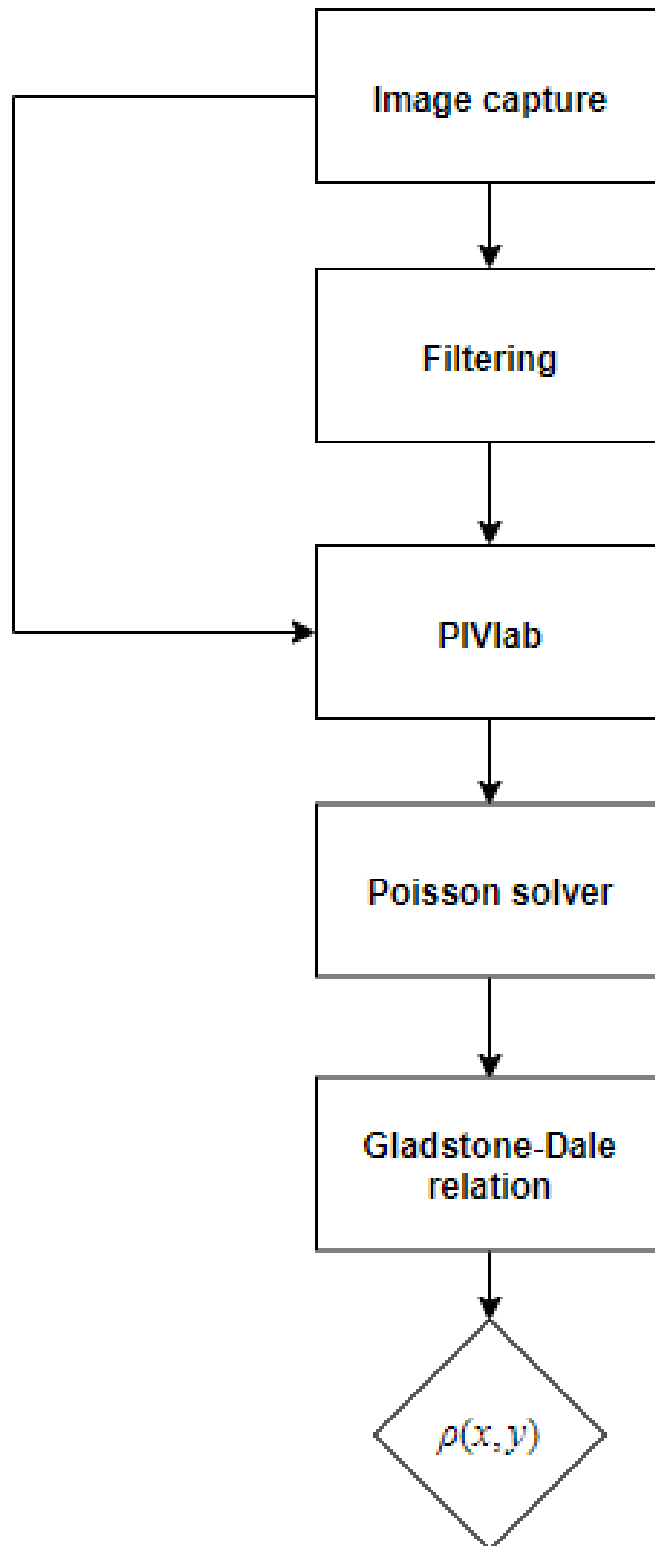
Figure 7.2.3: Flow chart of the procedure

7.2.2 Schlieren Study

A white LED was used as the light source for the Schlieren photography. The camera settings for the Schlieren gas jet analysis can be seen in Table 7.2.4. The razor was aligned horizontally for all Schlieren tests, so the shading gradients observed in the images captured are a result of the vertical density gradients.

Table 7.2.4: Camera Settings

Setting	
Frame Rate [pic/s]	40 000
Shutter Speed [s]	1/2700000
Resolution [pxl]	512 x 528
Pixel to mm conversion [pxl/mm]	0.297

Image analysis

The Schlieren images of the gas injections were all analyzed using a Matlab script made by co-supervisor Vladimir Krivopolianskii. By using this script one is able to obtain the gas jet penetration length and cone angle for each frame. Each pixel in each frame is assigned a value between 1 and 0 according to light intensity where 0 is black and 1 is white. A threshold value is specified by the user and according to this, the greyscale images are converted into black and white images. Every pixel with a value higher than the threshold is characterized as white, while every pixel with a lower value is characterized as black. For the analysis of all frames conducted in this study the threshold was set to 0.4.

The perceived geometry of the jet is determined by looking for the edges in the extremities of the jet. This is done by canny edge detection, meaning that the script is searching for the points where the pixel values turns from one to zero or from zero to one. Figure 7.2.4 shows a comparison between a raw image of an injection and the corresponding analyzed image with cone angle and jet penetration displayed.

Due to the compressible nature of the gas and some inertial effects in the needle lift mechanism, the first images in each series are captured before any jet propagation occurs. This resulted in the first frames being subject to noisy measurements. These frames were cut out from further analysis.

An analysis of the shockwave structure of the fully developed jet was carried out manually and qualitatively.

(a) Schlieren image of injection

Tested fuel = Nitrogen
BW border = 0.4
Edge method = canny

Time of sample = 5.800ms

16.1°

76 mm
256 pixels
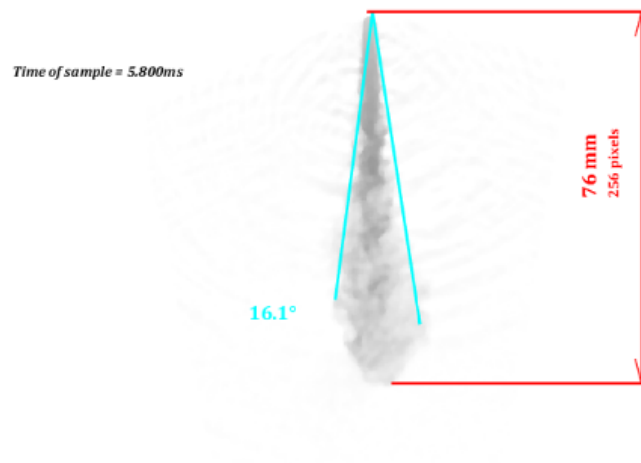
(b) Resulting analyzed image

Figure 7.2.4: Example of analyzed schlieren image

Chapter 8

Results and Discussion

In this chapter the findings and results of the study will be presented and discussed. Due to large amounts of data and sometimes similar trends for many of the experiments, relevant cases are used as representative examples for discussion. The influence of injector geometry, injection pressure and ambient pressure will be presented in plots and tables.

For the tests the lowest downstream-upstream NPR was 0.17. This is well below the critical limit for nitrogen of 0.53, so for all tests conducted the flow in question was choked. All pressures presented are absolute pressures.

8.1 Injector

In order to get valid results the characteristics of injector operation had to be determined. This section is dedicated to presenting the results of the injector performance in the tests outside the rig.

8.1.1 Needle-Lift Dynamics

The needle movement is a key parameter as it effectively determines the flow area of the injector. Knowing the flow area of the injector at all times during the injection process is a prerequisite for determining the injector operation profile. In Figure 8.1.1 the needle lift response for several different injection signal lengths are presented. For all tests there is a period of 21ms before any needle movement is registered. There is a known delay in the Hall effect sensor measuring needle lift of 18.75ms. This had been determined using a high speed camera during the preliminary study conducted in the fall of 2017.

(a) Needle lift steady-state

**(b)** Needle lift 60ms pulses

(c) Needle lift 30ms pulses
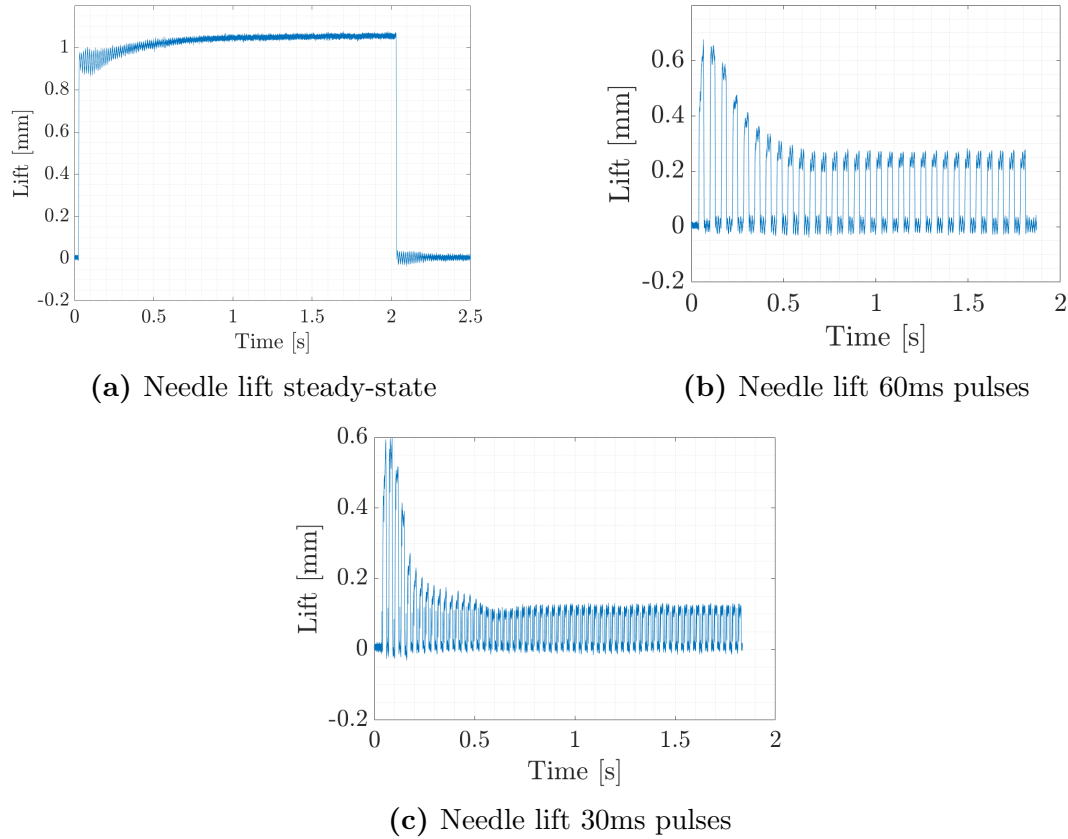
Figure 8.1.1: The needle lift for different pulse lengths

Figure 8.1.1a shows the needle lift from closed to fully lifted. The maximum needle lift is approximately 1.05mm. From the long pulse injection it is evident that the needle lift is not occuring at constant speed. Instead there is a rapid spike before an unsteady period of increase over the following 400-500ms. For the shorter pulses the maximum needle lift is 0.6mm and it decreases for each new repetition before stabilizing at 0.15mm for the 30ms pulses and 0.24mm for the 60ms pulses. From Figure4.2.2 it can be seen that the needle lift, not the nozzle area, is always the determining factor for the throat area for the stable region of the 30ms pulse tests.

Representative examples of the results of the tests to determine the needle dynamics of short single-shot injections can be seen in Figure 8.1.2.

(a) Needle lift. 2ms lift signal

(b) Needle lift. 6ms lift signal
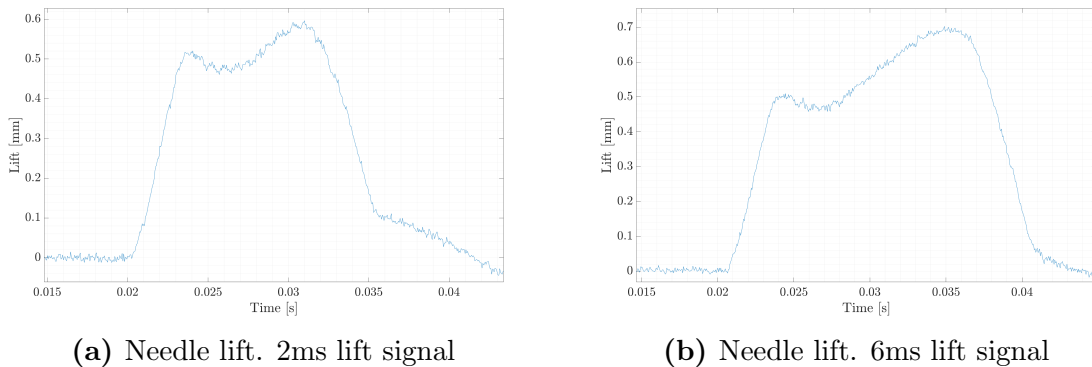
Figure 8.1.2: The needle lift for different pulse lengths

The observations show that the actuator does not manage to accurately follow the two injection pulse signals of 2ms and 6ms. For the 2ms injection signal test the time from closed-to-closed injector takes a total of 20ms.

The observations made reveals that there are some significant inertial effects in the hydraulic system performing the needle lift. The system fails in providing maximum needle lift for the shorter injection pulse signals. When subtracting the 18.75ms latency of the sensor,there is still a 2.25ms delay from the signal to the hydraulic servo valve until actual movement of the needle occurred. These slow responses are not critical problems for the purpose of testing in the laboratory, but this delay would not be acceptable for a fuel injector in an engine, where quick response and injection timing is paramount.

Even though the reference signal could not be followed, the deviations of the needle movement from test to test was small and therefore they were deemed successful in determining the needle dynamics.

8.1.2   Discharge Coefficients

It is important to note that the discharge coefficients calculated are not for the nozzle itself, but rather for the entire injector with the smallest flow area being the throat.

Steady-state

When conducting the steady-state tests, the needle was fully lifted at the time of sampling. Therefore, the nozzle area acted as the throat area. In order to cancel out the noisy measurements, the mean values of pressure, mass-flow and temperature in the steady-state interval were used for the calculation of the discharge coefficient. After extensive testing, the following discharge coefficients were found for the long pulse injections in the choked flow region.

**Table 8.1.1:** Discharge coefficients for steady-state flow

Nozzle geometry	Nozzle area $[mm^2]$	Cd [-]
Circular	1.720	0.9618
Circular	3.269	0.7812
Circular	6.514	0.4384
Double	1.720	0.9226
Triple	1.720	0.9126

As can be seen in Table 8.1.1 all of the the nozzles with smaller injection area performed significantly better than the largest nozzle in terms of losses. Upon further visual inspection it was discovered that the 2.88mm diameter nozzle was machined more roughly than the other four which might have resulted in large frictional losses.
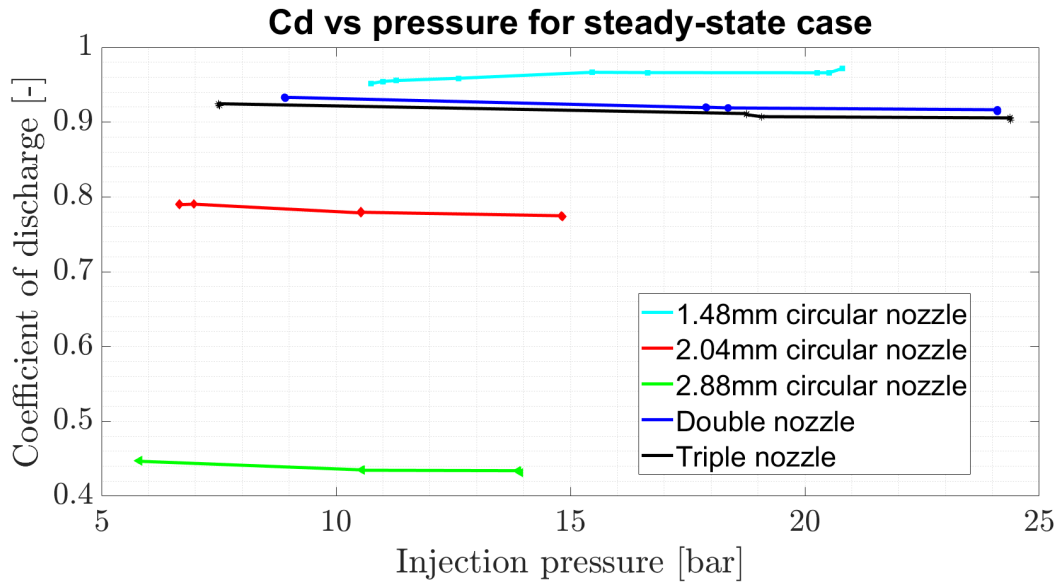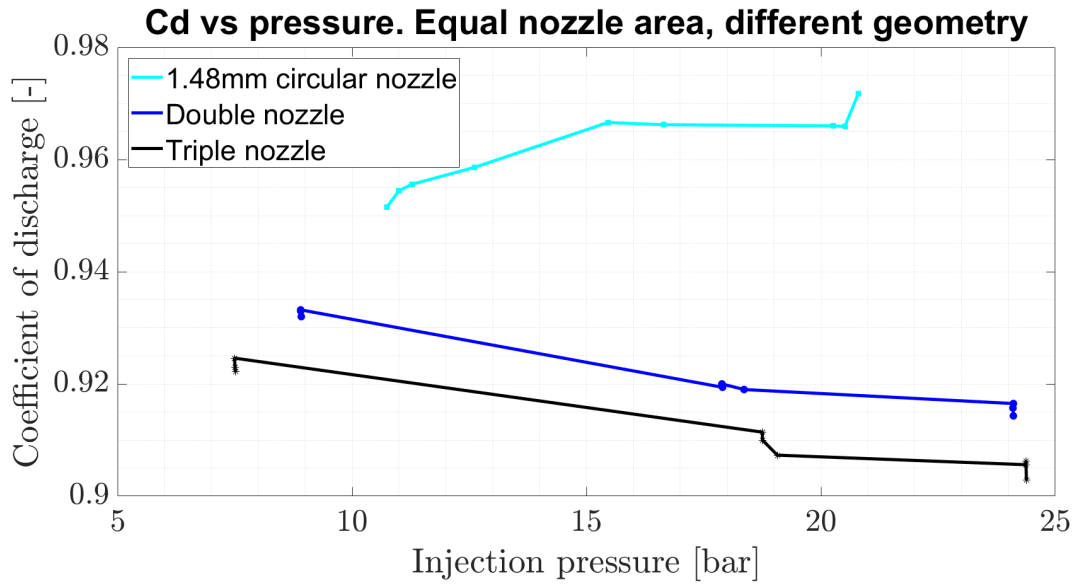
Figure 8.1.3: Discharge coefficient vs. injection pressure. All nozzles.

The effect of pressure ratio on the discharge coefficient was insignificant for the tests conducted in this study. The largest deviation was found in the coefficients for the 1.48mm circular nozzle. The difference between the highest and lowest values calculated was 2.08%. This can be attributed to measurement uncertainty. Equivalent results have been obtained in similar experiments. One of these is a study by Sridhara et al.[44]. They found that a decrease in downstream-upstream NPR would increase the discharge coefficient in the un-choked region, but not when the NPR was less than the critical value. The discharge coefficient is also highest in the supercritical range.
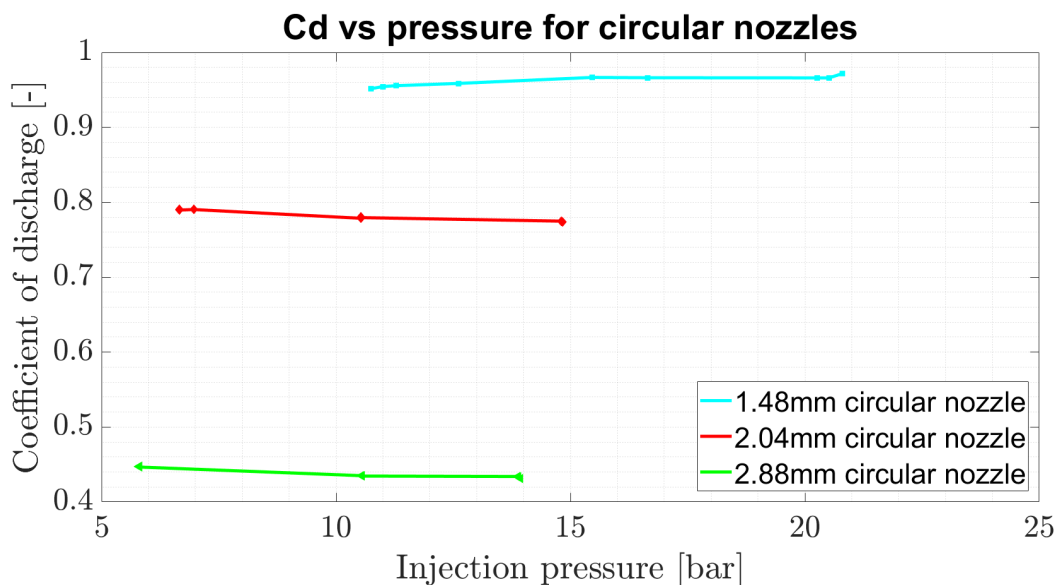

Figure 8.1.4: Discharge coefficient vs. injection pressure. Circular nozzles.

Figure 8.1.5: Discharge coefficient vs. injection pressure. Different shaped nozzles.

Figure 8.1.5 shows that the nozzles with the same area and different geometries performed similarly, but the more intricate geometries experienced slightly more losses. This might be due to the fact that the circumference of the nozzle opening is larger for the double and triple nozzle than for the circular nozzle. A larger circumference results in a larger internal surface area, and thus more surface for frictional forces to act.

Quasi steady-state

(a) Massflow
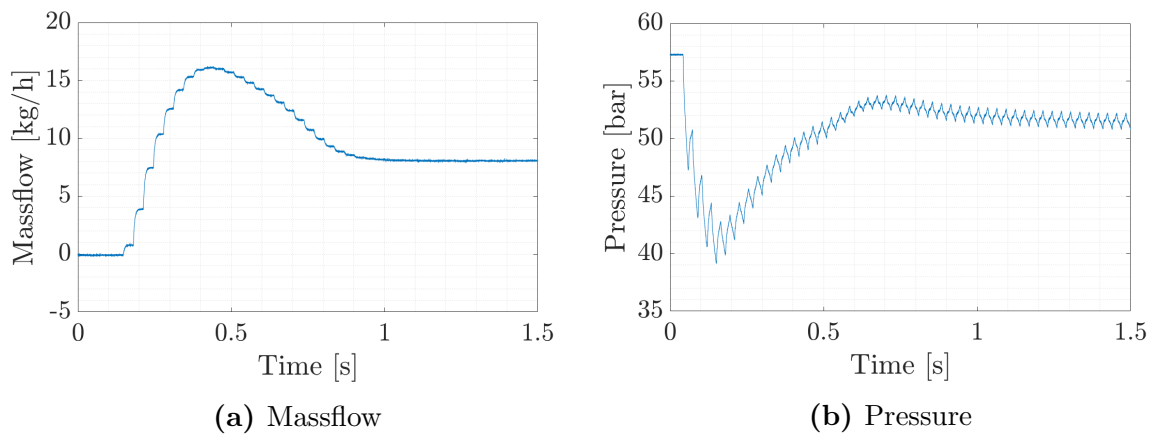
(b) Pressure

Figure 8.1.6: Pressure and massflow. 30ms pulses. 1.48mm circular nozzle

Figure 8.1.6 shows an example of the pressure and flow development for the rapid-burst experiments. Due to the compressible nature of the gas, the mass flow rate and pressure remained reasonably stable after a transient phase lasting until approximately 1 second into the injection.

For these tests the mass flow and flow area was integrated over the course of one needle-lift cycle in the time interval where the flow and pressure conditions had stabilized. These

integrated values were used to calculate the discharge coefficient for an entire injection pulse. Mass flow rate, pressure and temperature were assumed constant at the mean for the quasi-steady state region, despite small fluctuations.

Table 8.1.2 and Table 8.1.3 show the calculated discharge coefficients for the 60ms and 30ms pulses, respectively.

Table 8.1.2: Discharge coefficients obtained from 60ms pulses

Nozzle geometry	Nozzle area [mm^2]	Cd [-]
Circular	1.720	0.6270
Circular	3.269	0.3996
Circular	6.514	0.3410
Double	1.720	0.5578
Triple	1.720	0.5374

Table 8.1.3: Discharge coefficients obtained from 30ms pulses

Nozzle geometry	Nozzle area [mm^2]	Cd [-]
Circular	1.720	0.2791
Circular	3.269	0.2581
Circular	6.514	0.2431
Double	1.720	0.2672
Triple	1.720	0.2692

The discharge coefficient obtained for the dynamic experiments were significantly lower than the ones obtained from the tests with the injector fully opened. This indicates that the influence of the needle movement imposes extra resistance to the flow in the form of irreversible losses.

The smaller nozzles with higher discharge coefficients in the steady-state tests showed a more profound decrease in discharge coefficient, compared to the long pulse experiments, than the larger ones. The 1.48mm circular nozzle has a 71% decreased discharge coefficient when comparing the 30ms pulses to the steady-state case. The 2.88mm circular nozzle, on the other hand, only has a decrease of 45%. This can be attributed to the fact that the opening area of the needle acts as the throat area for much of the injection during these tests, in opposition to the long pulse shots where only the nozzle area was a contributing factor.

When comparing the maximum needle lift of the 30ms pulses, 0.15mm, to the values in Table 4.2.1 one can see that the nozzle areas of the 2.04mm and 2.88mm circular nozzles is larger than the area created by the needle lift for the entire pulse. Therefore, it never acts as the throat area. For the three nozzles with the smallest area, the nozzle area acts as the throat area only for a small fraction of the pulse. This is reflected in the results as the all discharge coefficients obtained from these tests were very similar, opposed to the ones obtained from the steady-state flow.

These results confirm that the throat area geometry effectively determines the discharge coefficient for a choked flow.

8.1.3 Injected Mass

The reason for establishing the discharge coefficients in the previous tests were to be able to determine the losses, and subsequently predict the injected mass for different injection durations and injection pressures. This was necessary because the mass flow meter was not reliable for such short bursts.

A rearrangement of the equation for discharge coefficient of choked flow, Eq.(4.2.3), was used to predict the injected mass for the different nozzles at different pressures and injection times. The result was the following equation:

$$m_{inj} = C_D \frac{P_u \sqrt{\kappa \frac{2}{\kappa+1}^{\frac{\kappa+1}{\kappa-1}}}}{\sqrt{RT}} \frac{\sum_{i=1}^{N_{samples}} A(i)}{v} \tag{8.1.1}$$

where v is the sampling frequency of the logging unit.

The model for predicting injected mass was a result of discrete integration of the nozzle area for an injection. The pressure and temperature was assumed to be constant. The temperature was assumed to be 20 °C as this was an approximation of the gas temperature in lab conditions. The temperature term is squared, and therefore does not have that much of an impact on the calculations. The needle movement was obtained from the data logged during the tests with short single-shot injections in the range of 2-10ms.

The discharge coefficients used were a weighted combination of the steady state discharge coefficient obtained from the two second injections and the discharge coefficient obtained for the 30ms bursts. The weighting was done according to how much of the injection time was controlled by nozzle area and how much was controlled by needle lift.
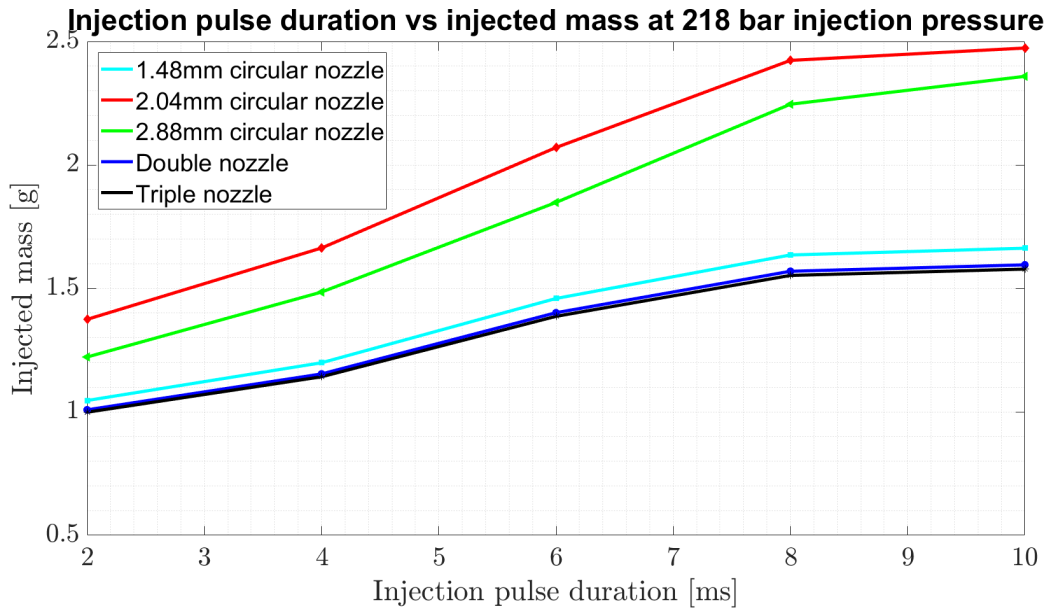
Figure 8.1.7: Injected mass at 218 bar
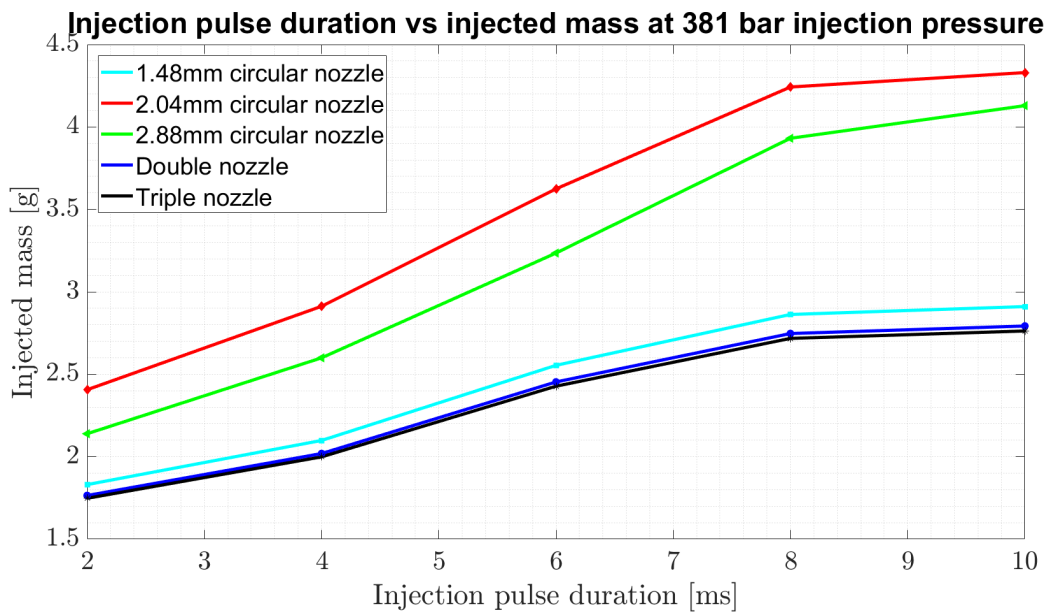
Figure 8.1.8: Injected mass at 381 bar

From Figure 8.1.7 and Figure 8.1.8 one can see that the 2.04mm circular nozzle delivers the most mass. It would have been expected that the nozzle with the largest area would have delivered the most mass, but due to the large losses, which are reflected in the low discharge coefficient, in the 2.88mm nozzle this potential increase in mass delivery is wasted.
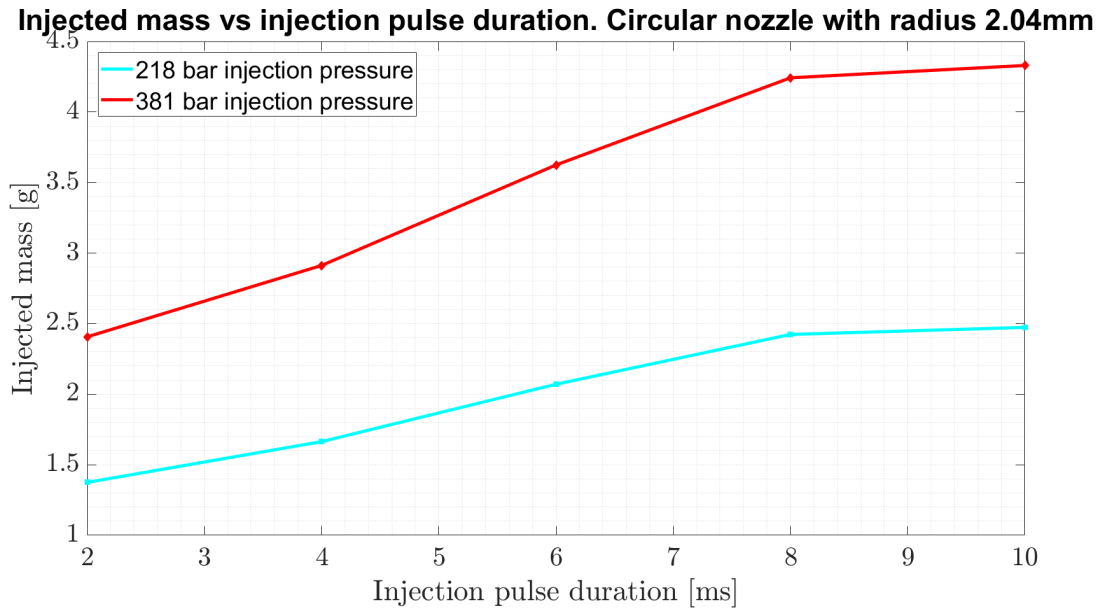
Figure 8.1.9: Injected mass for the 2.04mm nozzle

The model shows that in the choked region, the injection pressure influences the injected mass almost linearly. Experimental results from a study conducted by Dong et al. [25] also concludes with the gas fuel mass flow being linearly affected by injection pressure. The injected mass is independent of the chamber pressure for all relevant cases as the flow always will be choked.

A perfect model would take into account all of the different discharge coefficients for every needle position, but this was not possible. In reality there would also be a pressure drop as a consequence of the injection, but as the injections in the model were short, this pressure drop would be quite small and was therefore neglected.

The same model could be applied to obtain the injected mass if a combustible gas such as methane or hydrogen were used, as the discharge coefficient is linked to the injector geometry. One would only have to replace the properties that are specific to the species of gas used such as gas constant, R, and specific heats, C_P and C_v.

8.2   Gas Jet Characteristics

8.2.1   BOS

The results obtained in the BOS-tests show promise for future refinement, but are not satisfactory in their current state. The obtained displacement field appears to be accurate, but when applying the numerical solver to calculate the density field some abnormalities appear. For example: It can be see that a field of very low density appears right next to the jet.

The irregularities might be attributed to the Poisson solver struggling with finding the correct absolute values due to limited boundary conditions and stochastic effects caused by the dynamic and turbulent nature of the jet.

Tomographic reconstruction using the radon transform was attempted in order to improve the obtained density field, but did not yield any better results. Several other attempts were also made to modify the solving scheme and the test setup to eliminate the faulty analysis results. The effort to improve the results of the BOS-testing eventually had to be cut short due to time constraints. Figure 8.2.1 shows the steps in the BOS image analysis procedure.
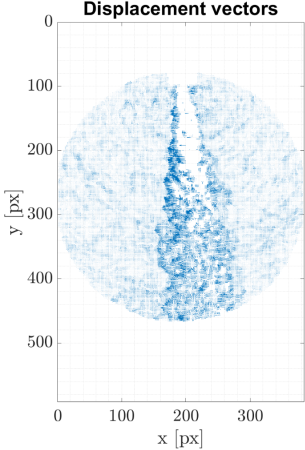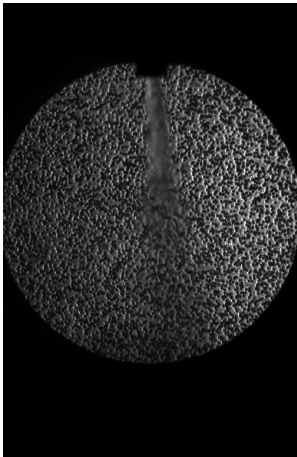
(a) Raw image of injection using BOS

(b) Displacement vectors obtained using PIV
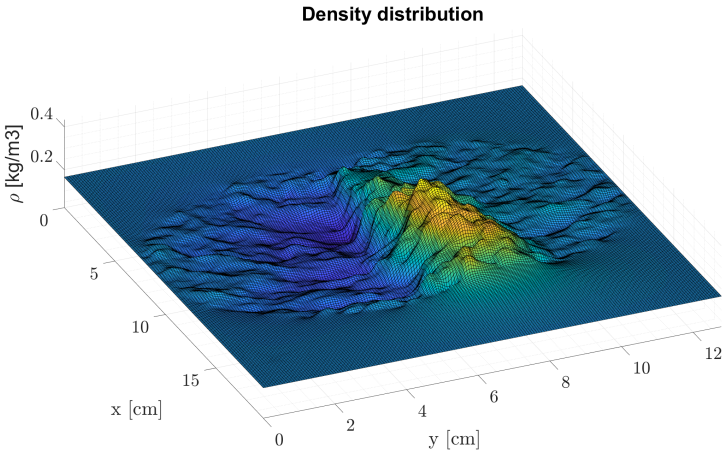
(c) Resulting density field

Figure 8.2.1: BOS process

8.2.2   Schlieren
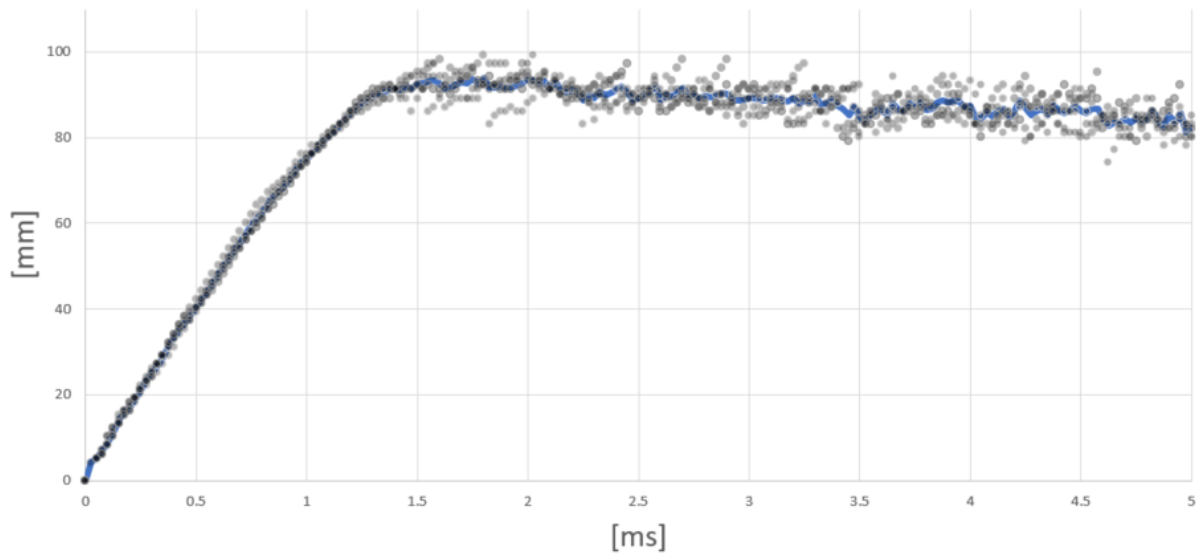
Figure 8.2.2:   Measured and averaged penetration length for 1.48mm circular nozzle.
Inj.Pressure:381bar.Ch.Pressure:20bar

Because of the before mentioned inconsistent injection- and chamber pressure, the pre-
sented values for both penetration length and cone angle are based on the averages of all
tests performed for each test case. This will, to a certain extent, remedy the effect of the
inconsistent boundary conditions. An example of such averaging can be seen in Figure
8.2.2 where the penetration lengths of all five shots with high injection pressure and high
chamber pressure for the 1.48mm circular nozzle can be seen. All of the measurements
follow the average almost perfectly until the jet reaches its fully developed state where
the deviations become more prevalent. The other test cases showed the same tendency.

To compensate for the inconsistency of the hydraulic servo valve and to more accurately
compare the jet developments, the data presented is from the first frame the injection is
visible. All data sets were checked and synchronized so that the start of injection was the
starting point for all data used for further consideration and discussion.

It proved to be difficult for the imaging tool to analyze the initial images, so the jet
propagation of the first few frames of the injection was lost for some of the tests. To
remedy this, each series of images was inspected manually in order to find the first frame
of injection and establish this as the start of injection. This means that even though
some data on the early stages of injection was lost, the validity of the data points that
are actually presented is not compromised. The problem of the analysis tool not being
able to detect the injection was especially prevalent for the injections with low chamber
pressure and low injection pressure, as these were the ones that produced the least stark
contrast.

Penetration length

All penetration length graphs can be seen in Appendix E.

## Penetratrion length, 2.88mm circular nozzle
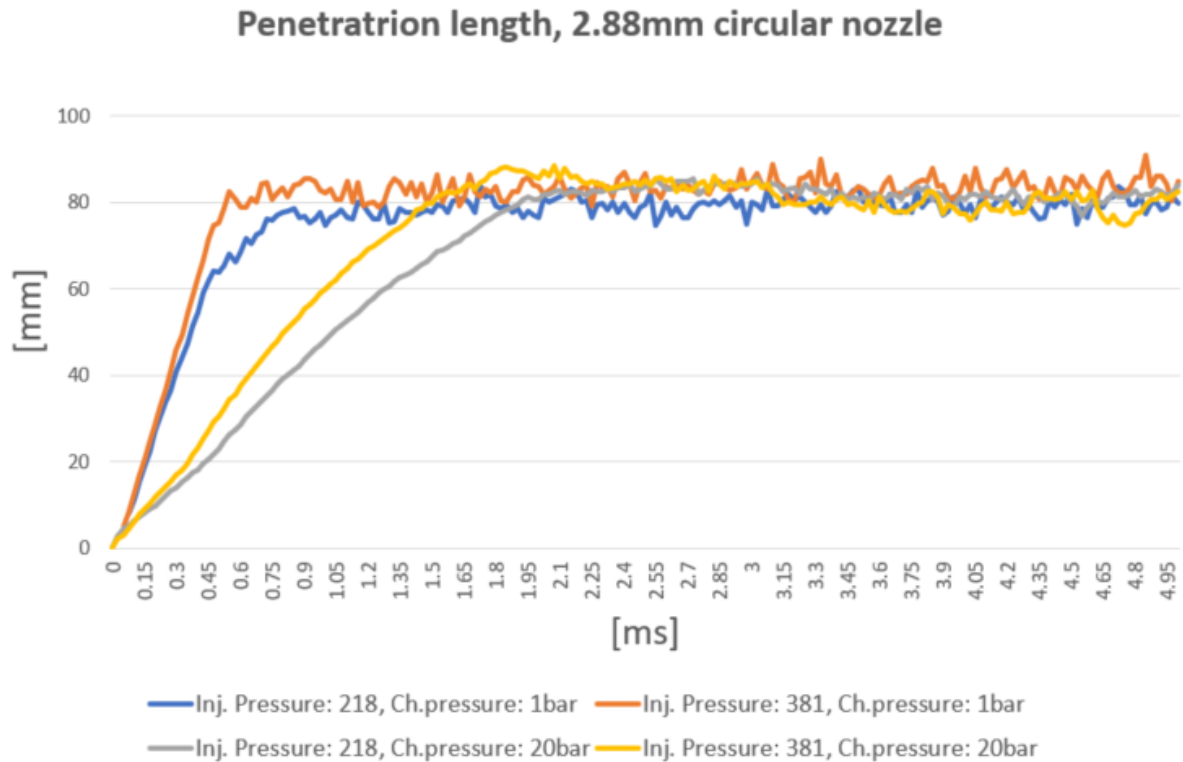
Figure 8.2.3: Jet penetration length for 2.88mm diameter circular nozzle

The results obtained in this study found that injection pressure had inconsequential effect on jet propagation velocity in the early phase of injection. Increased injection pressure did not result in equivalent increase in jet velocity. This coincides with the fact that the flow is choked, so the exit velocity of the jet is limited to local sonic velocity. Sonic velocity varies with temperature and to a certain extent pressure, but the difference will not be significant in the cases presented here. The same result was obtained by Dong et. al. [45].

Unlike the injection pressure, the chamber pressure did have a substantial effect on the gas jet propagation. The gas jets that were injected into the pressurized chamber experienced much larger resistance. By inspecting the slopes of the graph depicting jet penetration it can be seen that the jet speed of the injections done into the pressurized chamber are substantially lower. At 0.2ms into the injection the gas jets in the low-pressure chamber have a propagation of 27.2mm and 28.8mm, while the ones injected into the pressurized chamber had a penetration length of only 9.8mm and 11.8 mm. The increased chamber pressure reduces the jet propagation speed with 39% in the initial phase.

From the observations made, it would seem that the effect of NPR is less important to the jet penetration than the absolute value of the chamber pressure for a choked flow.
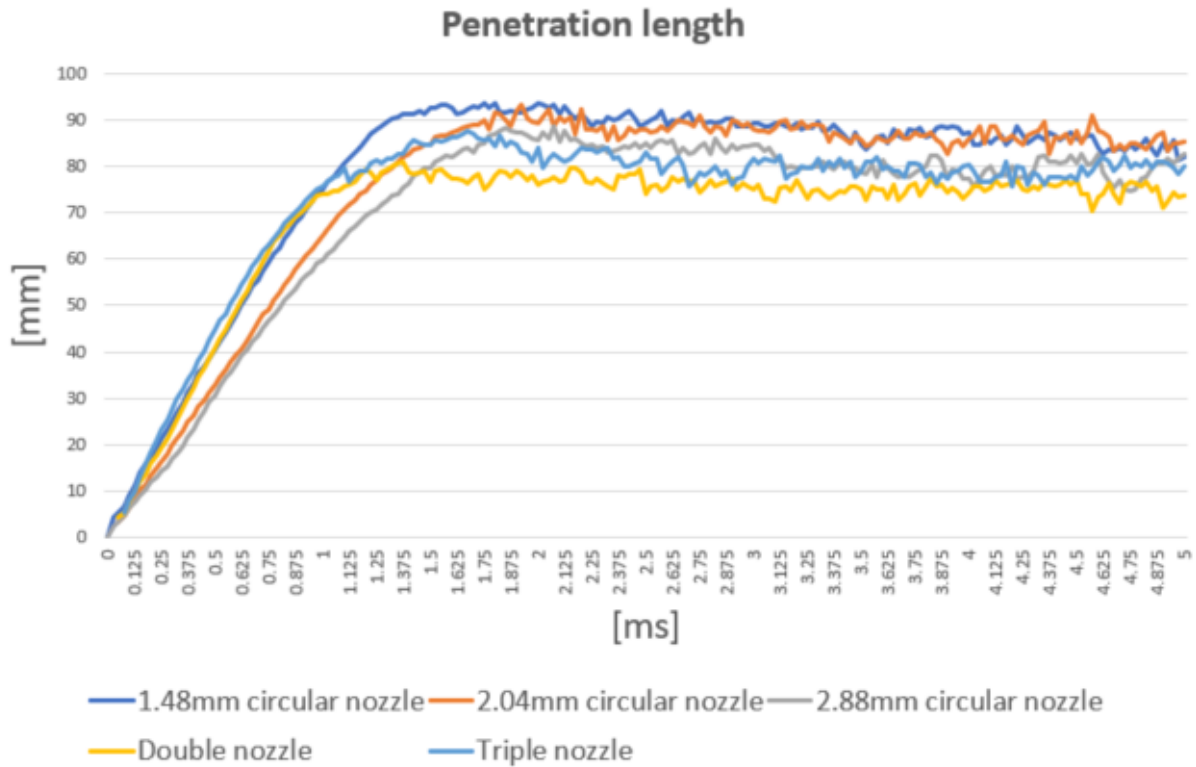
Figure 8.2.4: Penetration lengths for different nozzle geometries, Inj.Pressure:381bar, Ch.Pressure:20bar

Figure 8.2.4 shows a comparison of the penetration length development of the different nozzles at the same pressure conditions. The initial propagation shows that the nozzles with the smallest area provides a faster jet development. At 0.9ms into the injection the smallest nozzles with equal area have almost equal penetration length, independent of shape, while the larger ones have shorter penetration. At this point the smallest nozzles have an average penetration of 70.13mm. The 2.04mm diameter circular nozzle and the 2.88mm diameter circular nozzle have 15.3% shorter penetration and 21.0% shorter penetration, respectively.
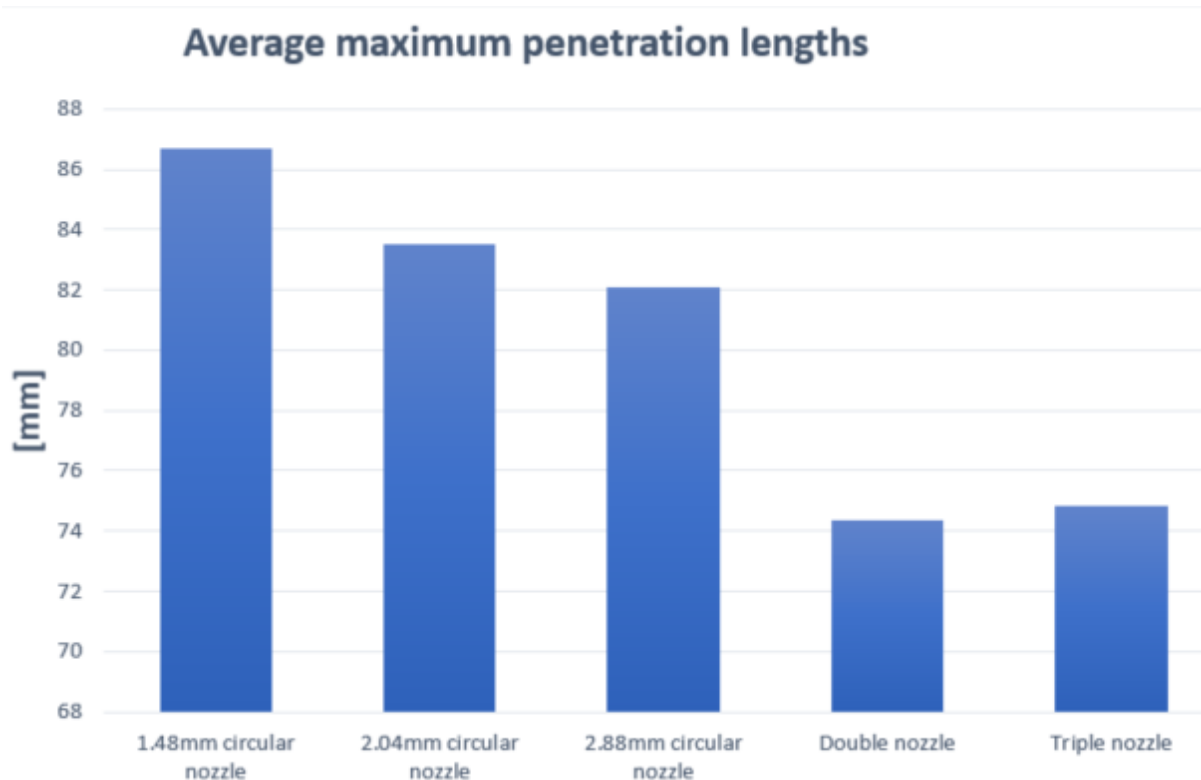
Figure 8.2.5: Maximum penetration lengths

The maximum penetration length, or the penetration length of the fully developed jet, was determined by averaging the penetration length values of 80 sample points in the time interval of 2ms to 4ms into the injection. This was done for each of the test cases and for the entire series of measurements, for each nozzle. The resulting average penetration lengths can be seen in Figure 8.2.5.

The nozzle geometry seemed to have substantial influence on the maximum penetration length. When the jets are fully developed, the circular nozzles display a longer maximum penetration length. The double and triple nozzle had nearly equal maximum average penetration length. Compared to the smallest circular nozzle, which had the same nozzle area, they had significantly shorter maximum penetrations.

In the dynamic phase of jet development, the jet propagation seems more dependent on nozzle size, while in the fully developed stage, the shape also played an important part.
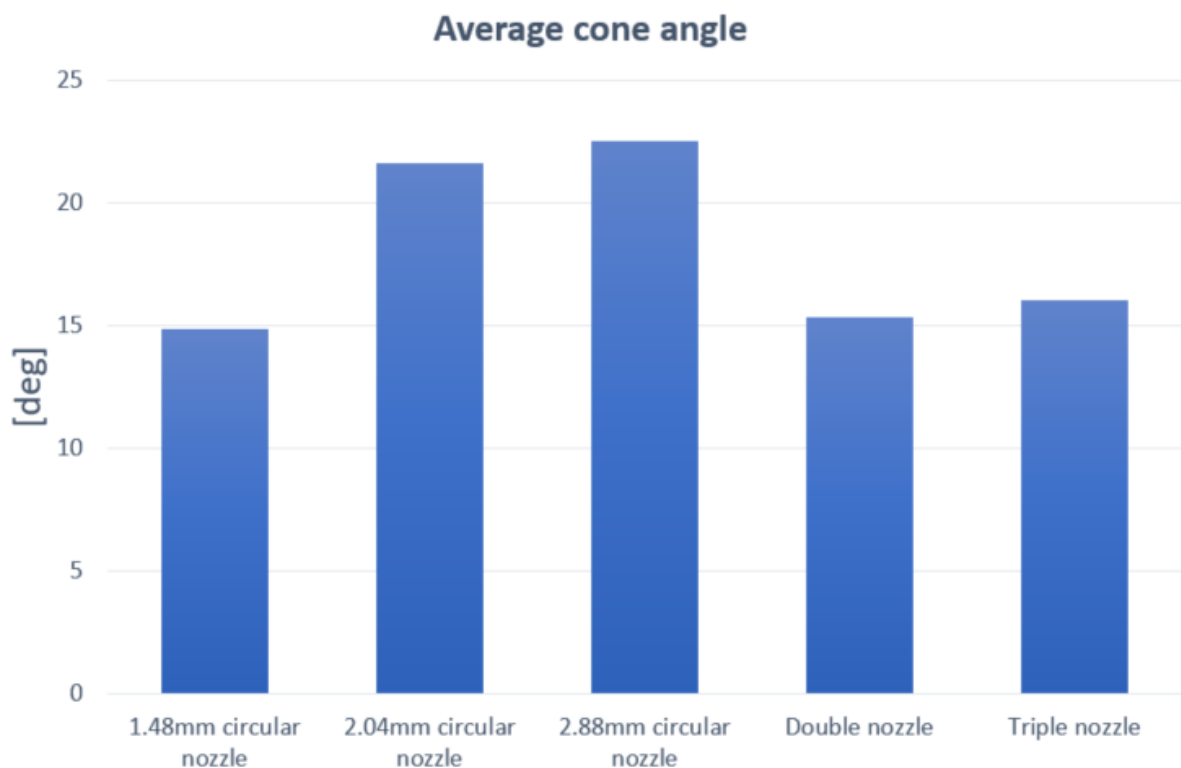
Cone angle

The results obtained from the study of cone angles turned out to be quite limited. Measurements were disturbed due to the confined space in which the injections took place. In the later frames of many of the injections the pressure waves propagating in the chamber become so strong that they are mistaken for the jet by the image analysis tool, resulting in an exaggerated cone angle. This is particularly prevalent in the tests with the pressurized chamber. An example of this development can be seen in Figure 8.2.6. Also, due to the image analysis tool's inability to recognize the gas jet for the first frames in almost every

injection, the information on the development of the cone angle at the very start of the injection was lost. Therefore, the basis of the results for the cone angle are a selection of frames from the region where stable and accurate measurements of the cone angle were made.
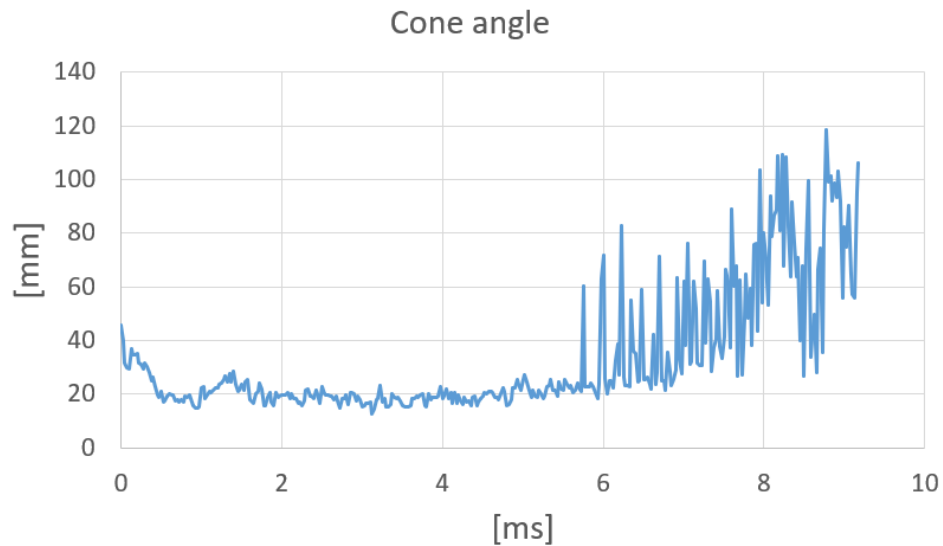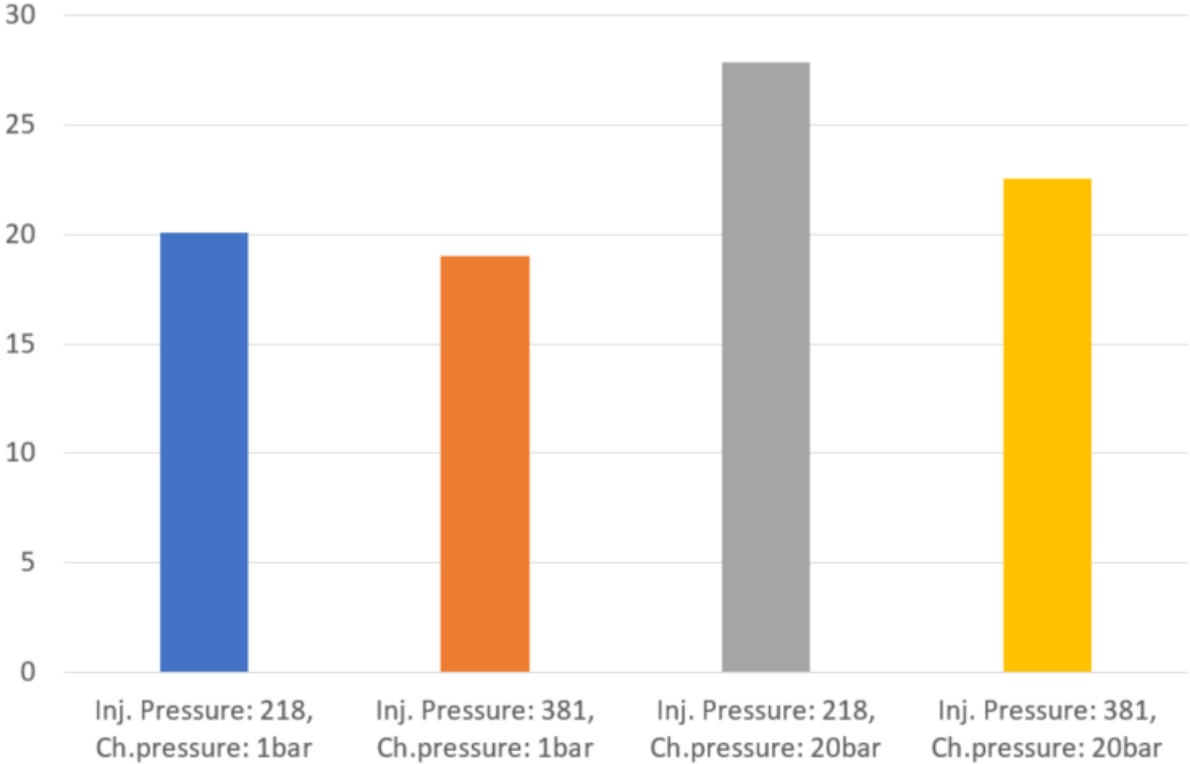

Figure 8.2.6: 2.04mm circular nozzle, Inj.Pressure:381bar, Ch.Pressure:20bar

Figure 8.2.7: Cone angles for high pressure injection and high chamber pressure

In Figure 8.2.7 the average cone angles for the different nozzles are presented. A sample of 100 frames picked from the time interval between 2ms and 3.5ms, where the cone angle

remained relatively stable, was chosen from each test scenario and the average is represented in the bar chart. The shape of the nozzle seems to have next to no impact on the cone angle, but increasing the nozzle area results in increased cone angle.

Figure 8.2.8: Cone angles. 2.88mm circular nozzle

In Figure 8.2.8 an example of cone angles for different pressure conditions can be seen. No clear connection could be drawn between injection pressure, chamber pressure and cone angle from the experiments performed. The results varied widely for the different nozzles. All cone angle measurements can be seen in Appendix F.

Dong et al.[45] found that increasing the injection pressure would increase the cone angle. In this study, only the three nozzles with the smallest area showed an increased cone angle with increasing injection pressure. The two other nozzles showed the exact opposite tendency, where increased injection pressure lead to a more narrow cone. All of the nozzles, except the 2.88mm circular nozzle showed reduced cone angles for higher chamber pressure at equal injection pressure. This contradicts the conclusion of Erfan et al.[46] who found that cone angle will increase with increased chamber pressure. Due to the inconsistency in the results obtained concerning the cone angle's dependency on pressure conditions, no conclusion can be drawn here.

Manual visual inspection
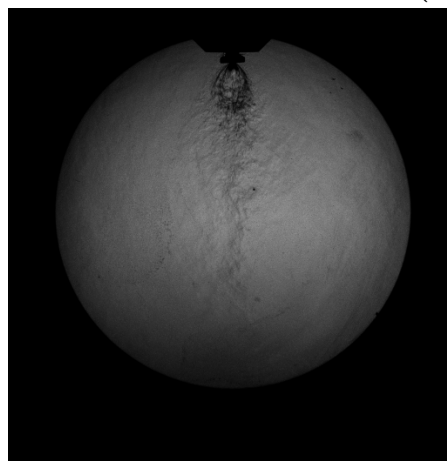

(a) 1.48mm circular nozzle

(b) 2.04mm circular nozzle

(c) 2.88mm circular nozzle

(d) Double nozzle

(e) Triple nozzle

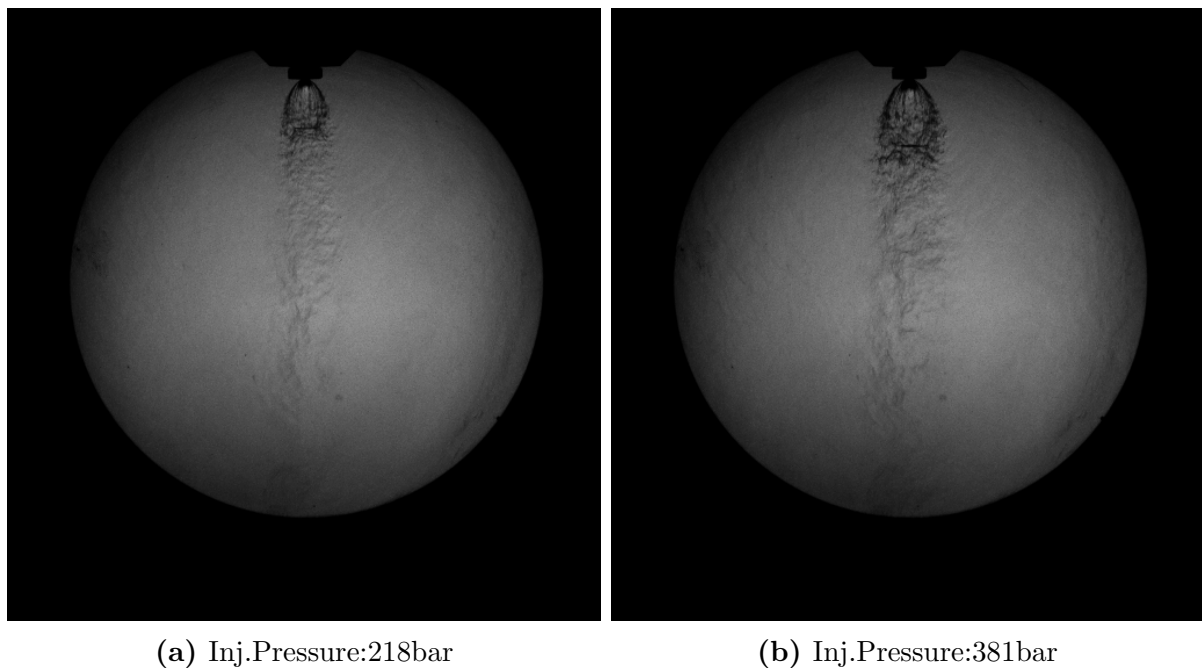**Figure 8.2.9:** Fully developed gas jet, Inj.Pressure:381bar, Ch.Pressure:1bar

In addition to the measurement of penetration length and cone angle, some interesting qualitative observations could made with the naked eye while inspecting the captured images. A series of Schlieren images depicting the gas jet development and propagation for the 1.48mm circular nozzle can be seen in Appendix D.

Figure 8.2.9 shows a comparison of the fully developed jets from all five nozzles. The injection conditions are practically equal at 381bar injection pressure and 1bar chamber pressure, so any observed differences in the gas jet geometry is caused by nozzle geometry. For all three cases the Mach disks are clearly visible. All jets are highly under-expanded. The smaller nozzles provided the widest Mach disk and the largest "bubble" caused by the barrel shock.

The shockwave structure of the double and triple nozzle show that they are affected by the non-axi-symmetrical geometry. The double nozzle show a line of increased density down the middle of the expansion section and the triple nozzle show a slight "bubble" in the middle. These are interesting phenomena, but it is difficult to extract any useful information based on this simple qualitative visual inspection alone. It would have been interesting to photograph the injections with the special nozzle designs at several different angles to get a better understanding of the 3D structure of the jet. A CFD model of this could also have provided interesting information.

(a) Inj.Pressure:218bar   (b) Inj.Pressure:381bar

Figure 8.2.10: Fully developed gas jet, 1.48mm circular nozzle, Ch.Pressure:20bar

Figure 8.2.10 shows the effect of injection pressure on the shock structure. Increasing the injection pressure also increased the size of the barrel shock and Mach disk. The increased injection pressure also increased the Mach disk height, which is in accordance with the model presented in Eq.(4.1.3)
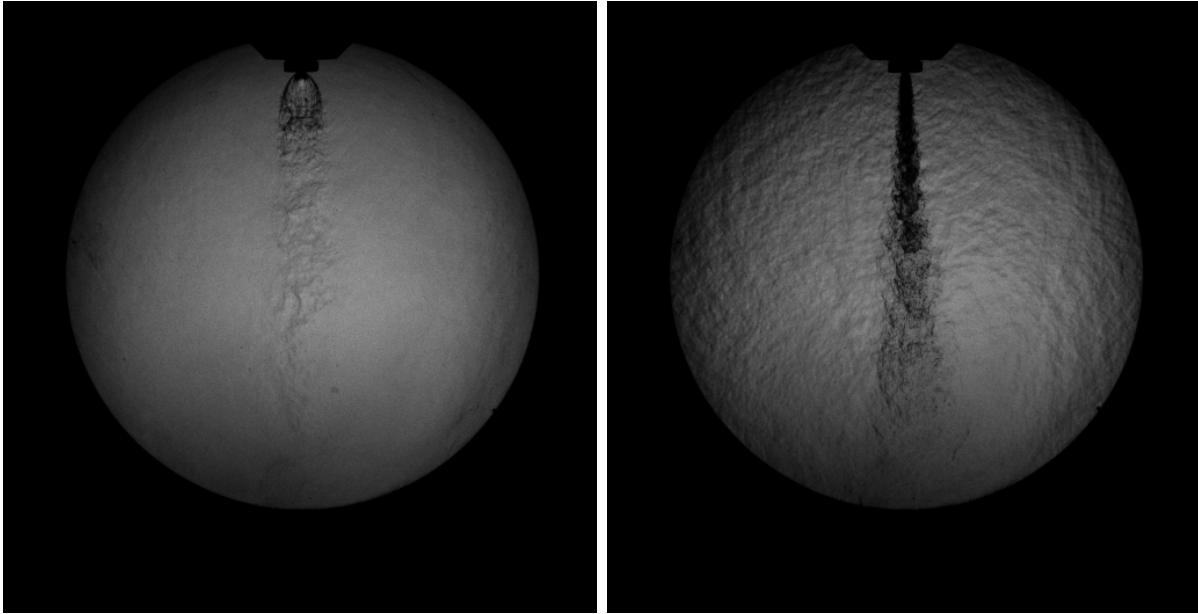
(a) Ch.Pressure:1bar   **(b)** Ch.Pressure:20bar

Figure 8.2.11: Fully developed gas jet, 1.48mm circular nozzle, Inj.Pressure:381bar

For the injections into the pressurized chamber, the shockwave structure of the gas jet was indiscernible as the density gradient was so large that the jet appeared as fully black, as can be seen in Figure 8.2.11. The increased chamber pressure has a obvious effect on the near-nozzle shock structure. The degree of under-expansion is severely decreased for the jet injected into the pressurized chamber compared to the one injected into the atmospheric pressure.

For a more in-depth study of the influence of nozzle geometry and chamber pressure on the shockwave structure, an image analysis tool designed specifically for this purpose would have to be made.

Chapter 9

Conclusion

9.1 Conclusion

The maritime industry has to change its practises if it is to comply with recent regulations and stay within acceptable limits of emissions of greenhouse gases, sulphur oxides, nitrogen oxides and particulate matter. Using alternative fuels with a cleaner emission profile than the much used heavy fuel oil, is one way to reduce emissions to an acceptable level. Of the potential alternative fuels, natural gas is the most viable as it is a proven and available solution. The increasing number of LNG-fuelled ships show that this is a concept that is catching on in the industry.

The different gas engine concepts all have their advantages and disadvantages. The HPDF engine reduces GHG emissions substantially both in comparison to conventional engines, due to 20-24% reduced CO_2 emissions(compared to MGO), but also compared to the other LNG engine concepts as it eliminates methane slip. The downside of this engine concept is the complex injection system and the more prominent NO_x formation (compared to other LNG engine concepts). A HPDF engine in combination with NO_x reduction measures such as EGR or SCR will be able to comply with tier III IMO regulations.

An experimental study with the purpose of determining the operation profile and characteristics of a new prototype single-hole gas injector was conducted. Optical methods were used to study the produced high pressure gas jet. Experiments were conducted both with steady-state flow conditions and for a dynamic rapid-bursts injection scenario and testing was done outside and inside of the CVCC.

Seeing as the injected medium and ambient gas in the CVCC was nitrogen, the quantitative data in this study might not be directly applicable to natural gas injection. The information obtained on the effects of nozzle geometry and pressure conditions on gas jet characteristics can still be applicable as they point to tendencies that may be similar or equal, independent of medium.

The discharge coefficients of the gas injector with the different nozzles for different operations were determined. For the steady-state conditions the smaller nozzles had a higher discharge coefficient, which means they experienced less frictional and contraction losses. The discharge coefficient for the fully opened injector in the choked flow region was: 0.96, 0.78 and 0.44 for the circular nozzles with diameter 1.48mm, 2.04mm and 2.88mm re-

---

spectively. The non-circular nozzles had a similar, but slightly lower discharge coefficient than the smallest circular nozzle, which had the same area.

The rapid burst tests showed the effect of the transient phase of needle lift on the discharge coefficient as the throat area was continually changing. These tests resulted in lower discharge coefficients than for the steady-state tests. For the shortest pulses, where the throat area was determined by needle lift for almost the entire pulse, the discharge coefficients were nearly equal, independent of nozzle.

A model for predicting the mass delivery of the injector was devised. This model showed that mass delivery was almost linearly dependent on the injection pressure, and the nozzle that provided most injected mass was the 2.04mm diameter circular nozzle. High injection pressure and a large nozzle area results in a greater mass flow, provided the nozzle is machined smoothly and does not experience too much loss.

The BOS study suffered from a number of non-physical phenomena appearing, which led to the results having to be discarded. Despite inconsistent results, a foundation has been laid for further work on applying the background-oriented schlieren technique in the laboratory.

For equal nozzle geometry, the increase of injection pressure is unable to obviously better the jet tip penetration due to the gas jet velocity being limited to the local sonic velocity by choking. Increasing the chamber pressure significantly slows down the gas jet propagation. In the dynamic phase, a smaller nozzle area provided the fastest jet propagation for equal pressure conditions. The jet penetration length of the fully developed jet was longer for the circular nozzles than for the double and triple nozzle. The longest maximum penetration length was obtained by the 1.48mm circular nozzle. No conclusive correlation was obtained between pressure conditions and cone angle, but the cone angle increased with increased nozzle area.

The results of this study indicate that a smoothly machined circular nozzle with large nozzle area at high injection pressure would result in the widest cone angle and provide the most mass in the shortest time. A smaller nozzle would provide a faster gas jet propagation, which facilitates good mixing, but the mass flow capacity would be reduced.

9.2   Recommendations for Further Work

As this is the first time this laboratory has been used for experimenting with gaseous fuels the research conducted was limited accordingly. Solid progress was made in upgrading the research facility and a basis has been laid for further research on high pressure injection and combustion.

Some more improvements of the research equipment would be beneficial. The most important thing would be to further improve the injector design to prevent leaks. The needle-lift mechanism using a hydraulic servo valve was not optimal, as the hydraulic system had a lot of inertia causing slow and delayed needle lift. It was still possible to obtain results, but a faster system, such as a solenoid valve, could generate a more rapid

response which would closer resemble the conditions in an injector used in a marine engine.

A natural progression would be to commence testing with natural gas injection in conjunction with a pilot fuel (biodiesel or MGO). Experiments with combustion would provide very useful data. It would reveal valuable information on the test parameters' effect on the rate of heat release and exhaust gas components. In other words, give a more complete understanding of the entire process and provide more applicable results.

Chamber design and injector placement are incredibly important features that affect the combustion. This is especially true in dual fuel engines where there are two injectors that operate in tandem, causing jet-spray-interaction. This is not possible to investigate properly with the current rig setup, but would be a beneficial continuation of the research.

Even though the results were not satisfactory this time, the BOS-experiments showed potential for being a valuable research tool in the lab in the future. More effort can be put into perfecting the test parameters such as camera settings, speckle pattern distribution, and the distances between background, test section and camera. The analysis script can also be further improved to better implement more accurate boundary conditions. One potential way to improve stability of the results is to use averages of multiple injections for further analysis.

If future Schlieren testing is to be performed, it will be beneficial to further improve the test setup and tune the image analysis script to avoid the loss of information during the early stages of injection.

Bibliography

[1] REN21 Secretariat. Renewables 2017 global status report. Technical report, Paris, France, 2017.

[2] J. J. Corbett, J. J. Winebrake, E. H. Green, P. Kasibhatla, V. Eyring, and A. Lauer. Mortality from ship emissions: a global assessment. Environmental science technology, 41, 2007.

[3] Working Groups I, II, and III to the Fifth Assessment Report of the Intergovernmental Panel on Climate Change. Climate change 2014 synthesis report. Technical report, Geneva, Switzerland, 2014.

[4] International Maritime Organization. Third imo ghg study 2014. Accessed from: http://www.imo.org/en/OurWork/Environment/PollutionPrevention/AirPollution/Pages/Greenhouse-Gas-Studies-2014.aspx (01.06.2018).

[5] United States Environmental Protection Agency. Particulate matter (pm) basics. Accessed from: https://www.epa.gov/pm-pollution/particulate-matter-pm-basicsPM (01.06.2018).

[6] V. Eyring, H. W. Köhler, J. van Aardenne, and A. Lauer. Emissions from international shipping: 1. the last 50 years. Journal of Geophysical Research: Atmospheres, 110, 2005.

[7] Z. Klimont, S. J. Smith, and J. Cofala. The last decade of global anthropogenic sulfurdioxide: 2000–2011 emissions. Technical report, 2013.

[8] International Maritime Organization. Nitrogen oxides (nox) – regulation 13. Accessed from: https://www.marpol-annex-vi.com/emissions/nitrogen-oxides-nox/ (23.05.2018).

[9] United States Environmental Protection Agency. Nitrogen oxides (nox), why and how they are controlled. Technical report, Research Triangle Park, North Carolina 27711, 1999.

[10] International Maritime Organization. Status of conventions. Accessed from: http://www.imo.org/en/About/Conventions/StatusOfConventions/Pages/Default.aspx (08.05.2018).

[11] International Maritime Organization. Sulphur oxides (sox) and particulate matter (pm) – regulation 14. Accessed from: http://www.imo.org/en/OurWork/environment/pollutionprevention/airpollution/pages/sulphur-oxides-(sox)-%E2%80%93-regulation-14.aspx (02.04.2018).

[12] International Maritime Organization. Energy efficiency measures. Accessed from: http://www.imo.org/en/OurWork/Environment/PollutionPrevention/AirPollution/ Pages/Technical-and-Operational-Measures.aspx (20.01.2018).

[13] W. T. Davies. Air pollution engineering manual. Wiley, 2 edition, 2000.

[14] M. M. Elgohary, I. S. Seddiek, and A. M. Salem. Overview of alternative fuels with emphasis on the potential of liquefied natural gas as future marine fuel. Journal of Engineering for the Maritime Environment, 229, 2014.

[15] A. A. Banawan, M. M. El Gohary, and I. S. Sadek. Environmental and economical benefits of changing from marine diesel oil to natural-gas fuel for short-voyage high-power passenger ships. Journal of Engineering for the Maritime Environment, 224, 2010.

[16] M. L. Andersen P. C. Sames, N. B. Clausen. Costs and benefits of lng as ship fuel for container vessels. Technical report, Copenhagen, Denmark, 2012.

[17] G.M. Wuersig, A. Chiotopoulos, and S. Adams. In focus - lng as ship fuel: Latest developments and projects in the lng industry. Technical report, Hamburg, Germany, 2016.

[18] C. Robinson and D. B. Smith. The auto-ignition temperature of methane. Journal of Hazardous Materials, 8, 1984.

[19] D. Stenersen and O. Thonstad. Ghg and NO_x emissions from gas fuelled engines. 2017.

[20] A. Hajialimohammadi, D. Edgington-Mitchell, D. Honnery, N. Montazerin, A. Abdullah, and M. A. Mirsalim. Ultra high-speed investigation of gaseous jet injected by a single-hole injector and proposing of an analytical method for pressure loss prediction during transient injection. Fuel, 184, 2016.

[21] P. G. Hill and P. Ouellette. Transient turbulent gaseous fuel jets for diesel engines. Journal of Fluids Engineering, 121, 1999.

[22] P. G. Hill and C. L. Peterson. Mechanics and thermodynamics of propulsion. Addison-Wesley Publishing Company, 1995.

[23] National Aeronautics and Space Administration (NASA). Mass flow choking. Accessed from: https://www.grc.nasa.gov/www/k-12/airplane/mflchk.html (03.06.2018).

[24] D. Edgington-Mitchell, D. R. Honnery, and J. Soria. The underexpanded jet mach disk and its associated shear layer. Physics of fluids, 26, 2014.

[25] Q. Dong, Y. Li, E. Song, C. Yao, L. Fan, and J. Sun. The characteristic analysis of high-pressure gas jets for natural gas engine based on shock wave structure. Energy Conversion and Management, 149, 2017.

[26] H. Ashkenas and F. S. Sherman. Structure and utilization of supersonic free jets in low density wind tunnels. Technical report, Jet Propulsion Lab., California Inst. of Tech.; Pasadena, CA, United States, 1965.

[27] M.M.A. Alama, T. Setoguchia, S. Matsuob, and H.D. Kim. Nozzle geometry variations on the discharge coefficient. Propulsion and Power Research, 5, 2016.

[28] B. T. Miralles. Preliminary considerations in the use of industrial sonic nozzles. Flow Measurement and Instrumentation, 11, 1999.

[29] E. Pedersen and H. Engja. TMR4275 Modelling, Simulation and Analysis of Dynamic Systems. Institutt for marin teknikk, Fakultet for ingeniørvitenskap og teknologi, NTNU, 2008.

[30] A. Davidhazy. Introduction to shadowgraph and schlieren imaging(2006). Accessed from: http://scholarworks.rit.edu/article/478 (02.03.2018).

[31] G. S. Settles. Schlieren and Shadowgraph Techniques. Springer, 2001.

[32] U. Wernekinck and W. Merzkirch. Speckle photography of spatially extended refractive-index fields. Appl. Opt., 26(1):31–32, 1987.

[33] G.E.A. Meier. Computerized background-oriented schlieren. Experiments in Fluids, 33, 2002.

[34] H. Richard and M. Raffel. Principle and applications of the background oriented schlieren (bos) method. Measurement Science and Technology, 12, 2001.

[35] M. Raffel. Background-oriented schlieren (bos) techniques. Experiments in Fluids, 56, 2014.

[36] E. Ramsden. Hall-effect sensors: theory and applications. Elsevier, 2.nd edition, 2006.

[37] M. Gritsch, C. Saumweber, A. Schulz, S. Wittig, and E. Sharp. Effect of internal coolant crossflow orientation on the discharge coefficient of shaped film-cooling holes. Journal of Turbomachinery, 122, 2000.

[38] Engine Combustion Network. "spray a" and "spray b" operating condition. https://ecn.sandia.gov/diesel-spray-combustion/target-condition/spray-ab/ (08.06.2018).

[39] W. Thielicke and E.J. Stamhuis. Pivlab – towards user-friendly, affordable and accurate digital particle image velocimetry in matlab. Journal of Open Research Software, 30, 2014.

[40] W. Thielicke. The flapping flight of birds - analysis and application. phd thesis, rijksuniversiteit groningen. Accessed from: http://irs.ub.rug.nl/ppn/382783069 (15.04.2018).

[41] L. Verso and A. Liberzon. Background oriented schlieren in a density stratified fluid. Review of Scientific Instruments, 86, 2015.

[42] Thorlabs Inc. Optical substrates. Accessed from: https://www.thorlabs.com (28.04.2018).

[43] E. Kreysig. Advanced Engineering Mathematics. Wiley, 10 edition, 2011.

[44] K. S. Hebbar, K. Sridhara, and P. A. Paranjpe. Performance of conical jet nozzles in terms of discharge coefficient. Journal of the Aeronautical Society of India, 22, 1970.

[45] Q. Dong, Y. Li, E. Song, C. Yao, L. Fan, and J. Sun. Visualization research on injection characteristics of high-pressure gas jets for natural gas engine. Applied Thermal Engineering, 132, 2018.

[46] I. Erfan, A. Hajialimohammadib, I. Chitsazc, M. Ziabasharhaghd, and R. J. Martinuzz. Influence of chamber pressure on cng jet characteristics of a multi-hole high pressure injector. Fuel, 197, 2017.

Appendix A: Injector Nozzle Geometry
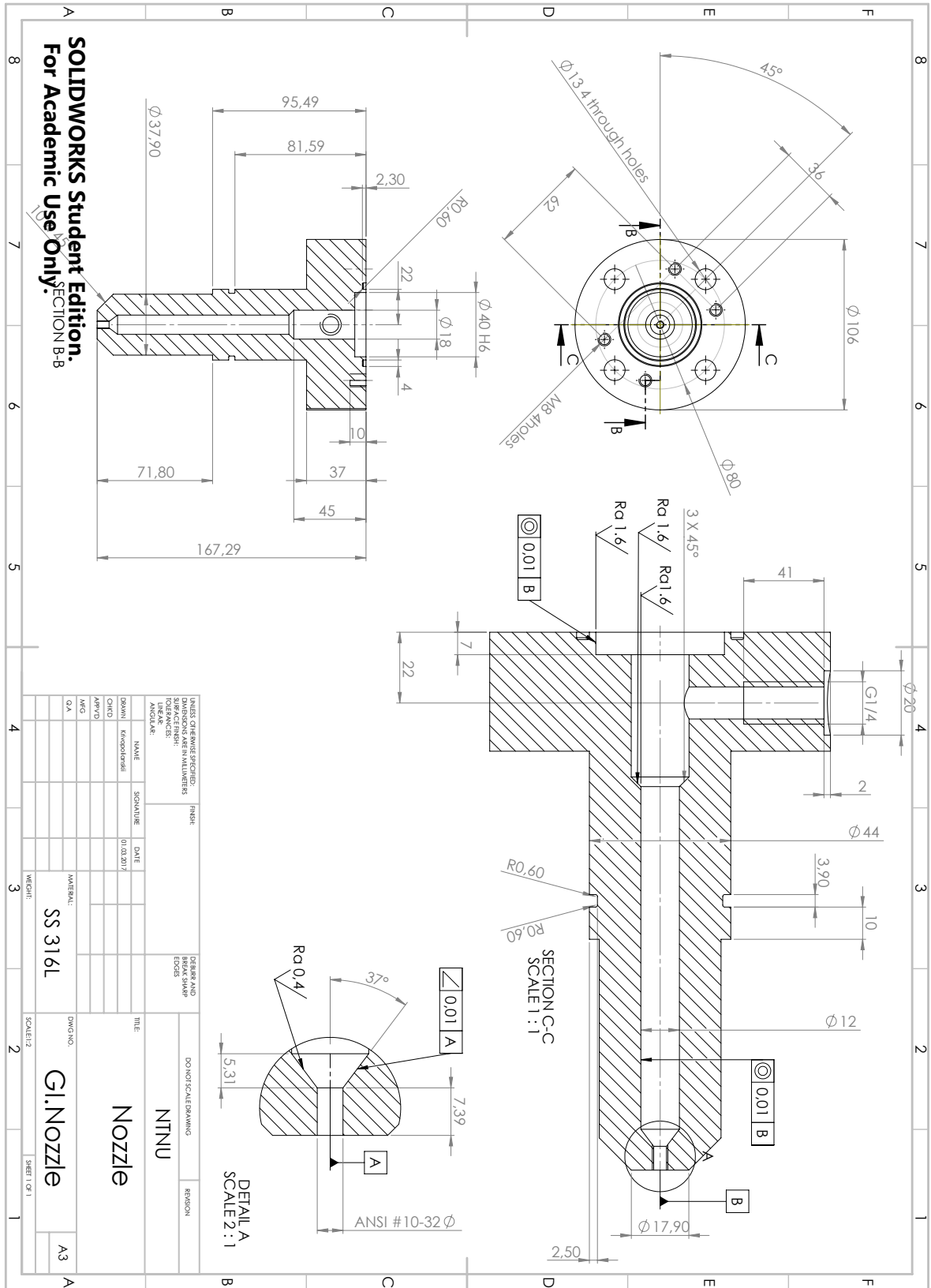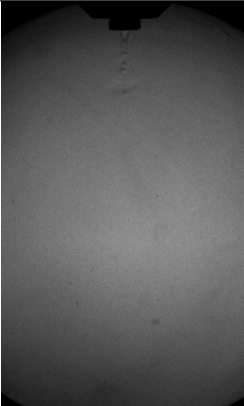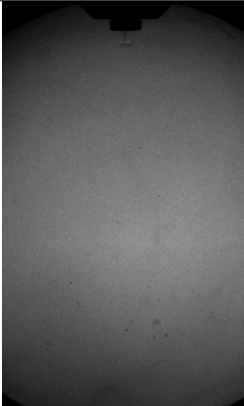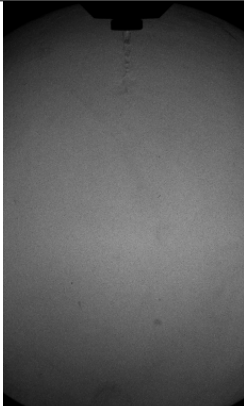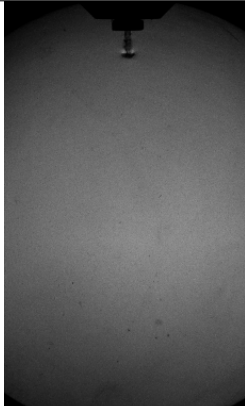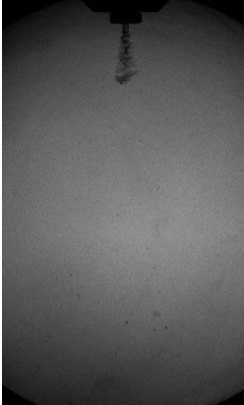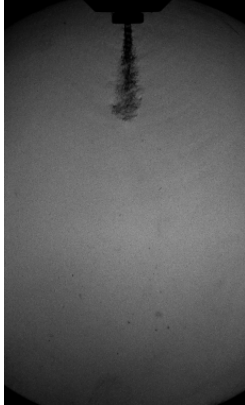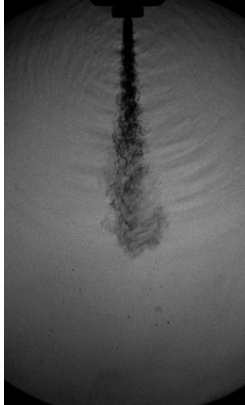
Appendix B: Injector Needle Geometry
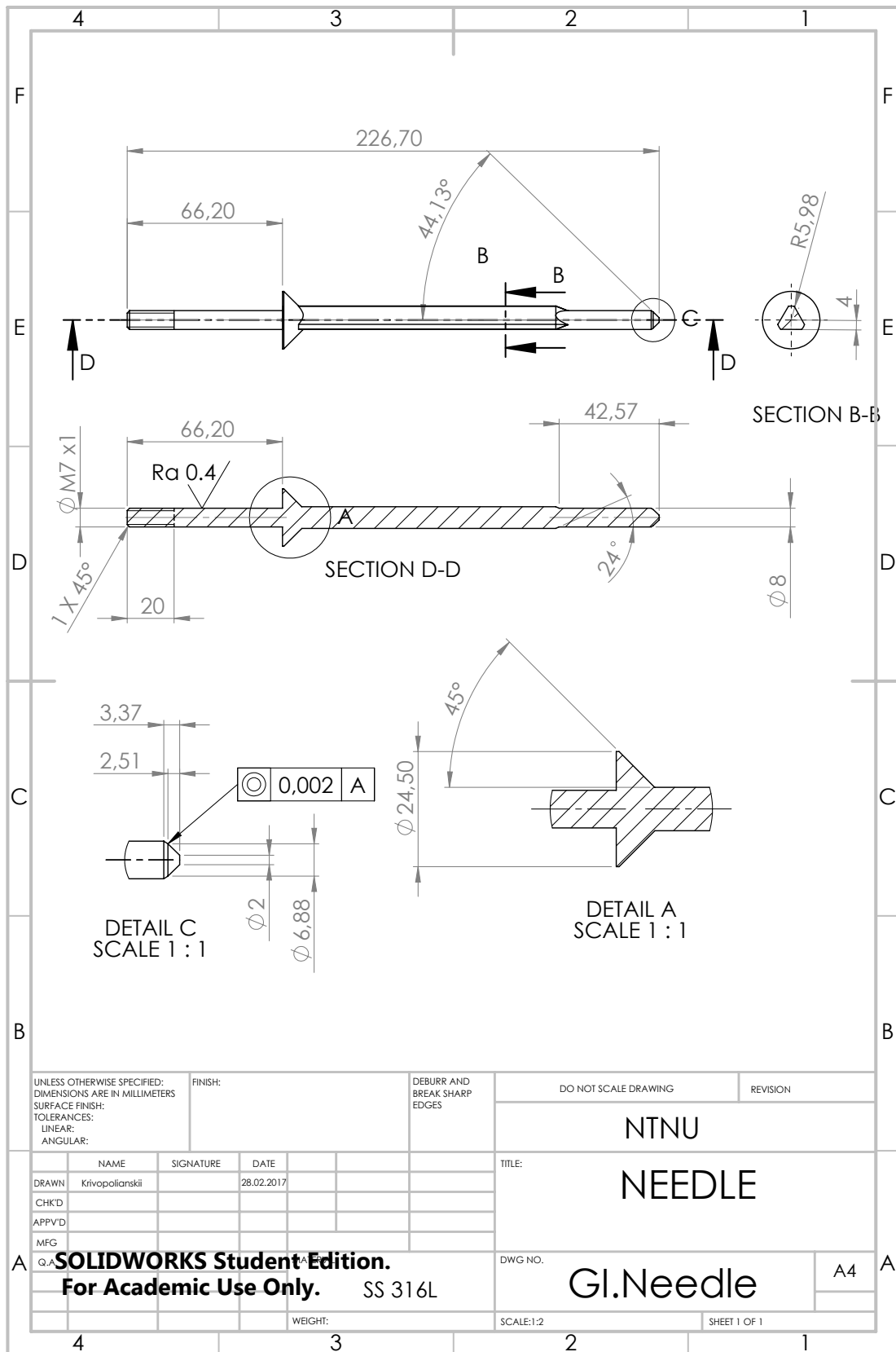
Appendix C: Measure Protocol example
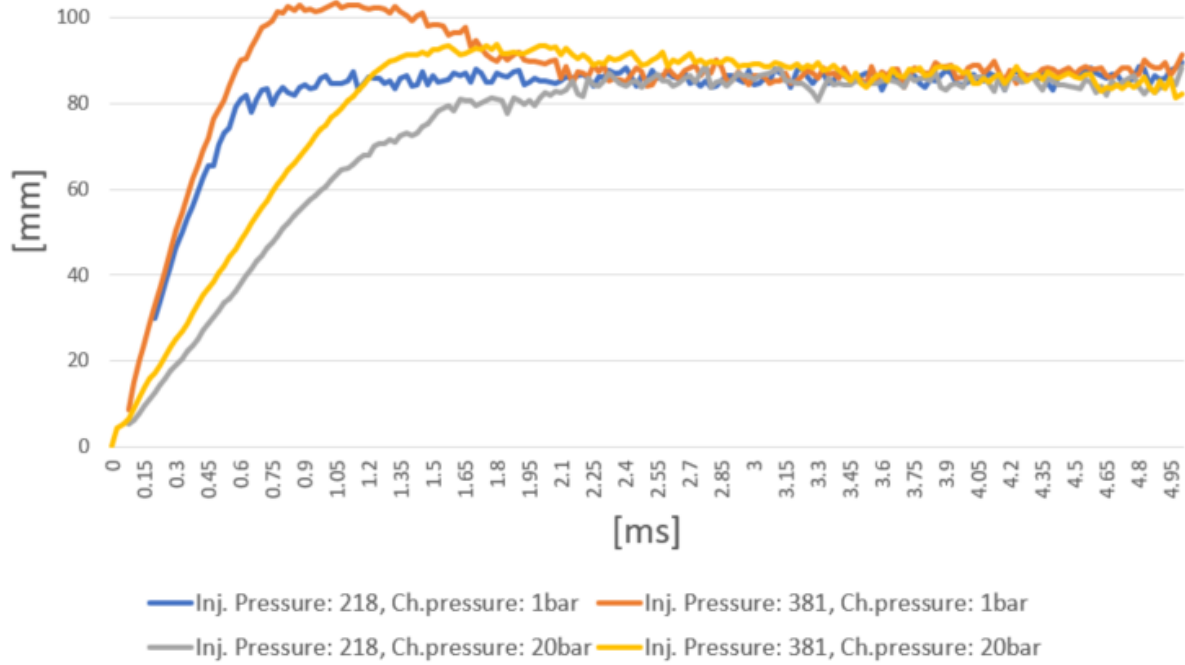
Measure Protocol 124				High Pressure Injection	
Keyword	High pressure nitrogen injection, BOS				
Protocol number	124				
Injector	Prototype gas injector				
Nozzle	Circular				
Injector number	-				
Imaging technique	Background-oriented schlieren				
Nozzle Area	3.27	[mm2]	Injection signal time	2000	[µs]
Number of holes	1	[-]	Injection Temp	-	[°C]
Spray angle	-	[°]	Exposure	-	microsec
Room temp.	22	[°C]	Shutter time	1/400000	[s]
Fuel Pressure	200-400	bar	Pictures	750	[-]
Frame Rate	40000	p/s	Time of P-r star	-	[s]
Resolution	384x592	[pxl]	Speed of fan	-	rpm
Point	Chamber pressure		Injection pressure		Chamber temperature
[-]	[bar]		[bar]		[°C]
1	1.1		221.0		23
2	1.1		221.8		23
3	1.0		219.5		23
4	1.1		220.3		23
5	1.1		220.5		23
6	19.9		219.4		23
7	20.2		220.8		23
8	20.0		220.9		23
9	20.3		220.3		23
10	20.5		219.7		23
11	1.1		387.7		23
12	1.1		382.0		23
13	1.1		381.9		23
14	1.0		379.2		22
15	1.0		381.6		23
16	20.2		386.5		23
17	20.3		387.5		23
18	20.5		387.0		23
19	21.2		388.2		23
20	21.3		377.7		22
Comments					
Operator	Bredahl				

Appendix D: Jet propagation. 1.48mm circular nozzle

Inj.pressure[bar]	218		381	
Ch.pressure[bar]	1	20	1	20

t = 0.125 ms

t = 0.375 ms

t = 0.875 ms

t = 1.625ms

Appendix E: Jet penetration length

Penetratrion length, 1.48mm circular nozzle

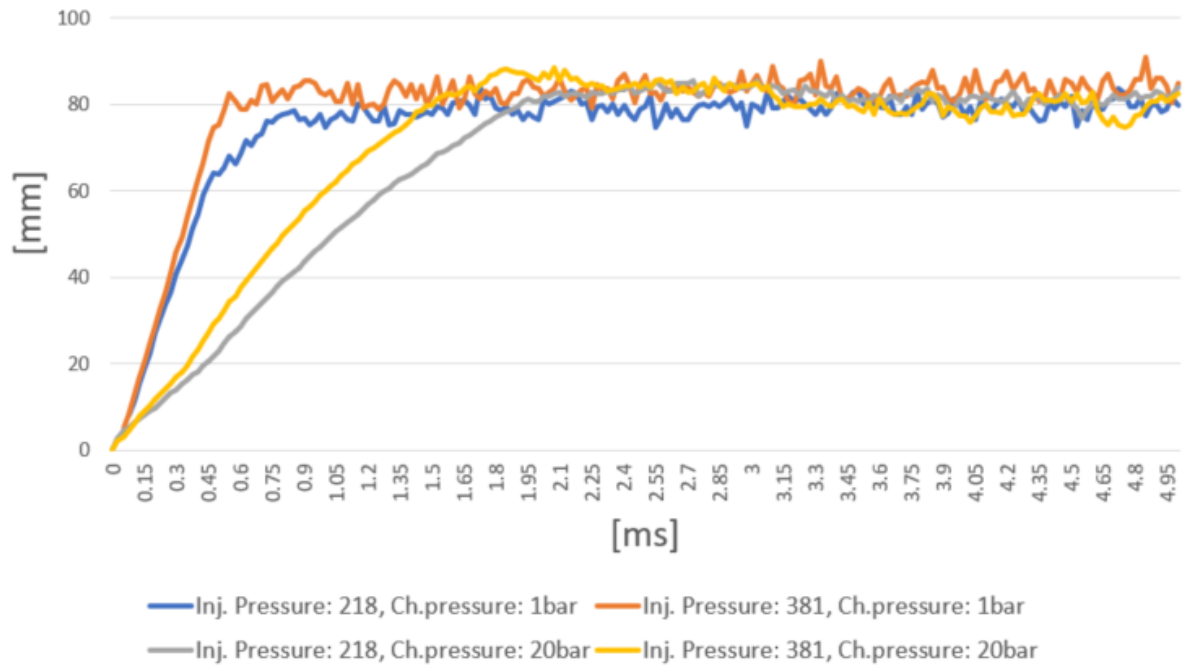
Legend:
— Inj. Pressure: 218, Ch.pressure: 1bar — Inj. Pressure: 381, Ch.pressure: 1bar
— Inj. Pressure: 218, Ch.pressure: 20bar — Inj. Pressure: 381, Ch.pressure: 20bar

Penetratrion length, 2.04mm circular nozzle

Legend:
— Inj. Pressure: 218, Ch.pressure: 1bar — Inj. Pressure: 381, Ch.pressure: 1bar
— Inj. Pressure: 218, Ch.pressure: 20bar — Inj. Pressure: 381, Ch.pressure: 20bar

Penetratrion length, 2.88mm circular nozzle

Legend:
— Inj. Pressure: 218, Ch.pressure: 1bar
— Inj. Pressure: 381, Ch.pressure: 1bar
— Inj. Pressure: 218, Ch.pressure: 20bar
— Inj. Pressure: 381, Ch.pressure: 20bar
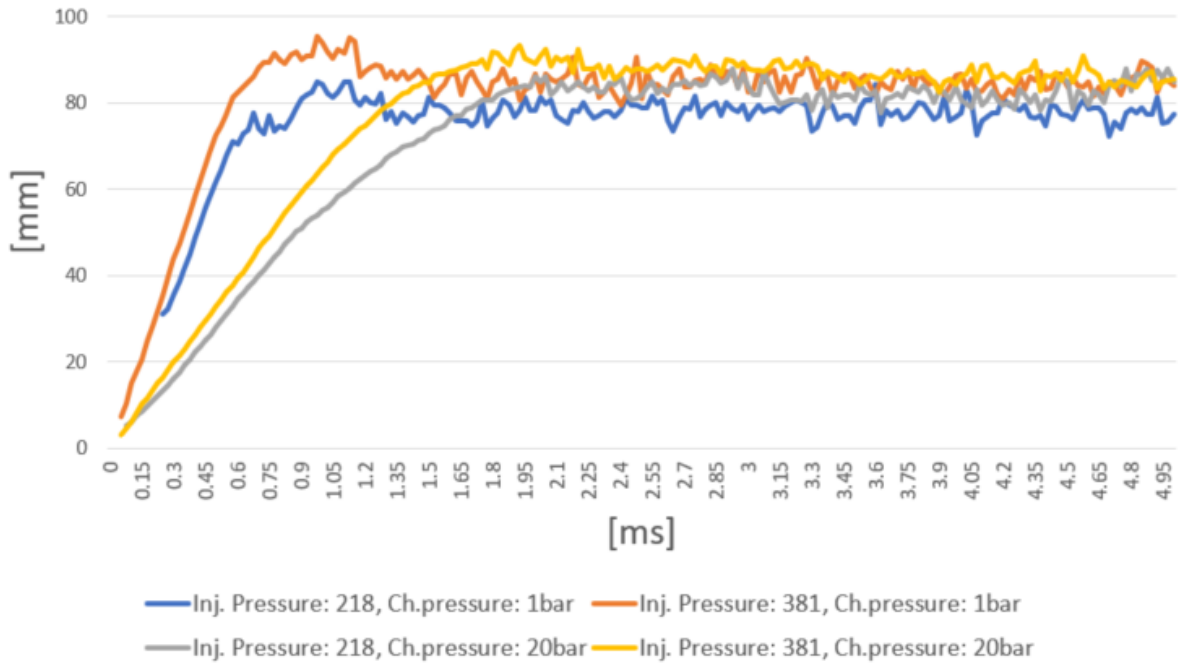
Penetratrion length, double nozzle

Legend:
— Inj. Pressure: 218, Ch.pressure: 1bar
— Inj. Pressure: 381, Ch.pressure: 1bar
— Inj. Pressure: 218, Ch.pressure: 20bar
— Inj. Pressure: 381, Ch.pressure: 20bar

Experimental Study of High Pressure Gas Injection Using Optical Methods
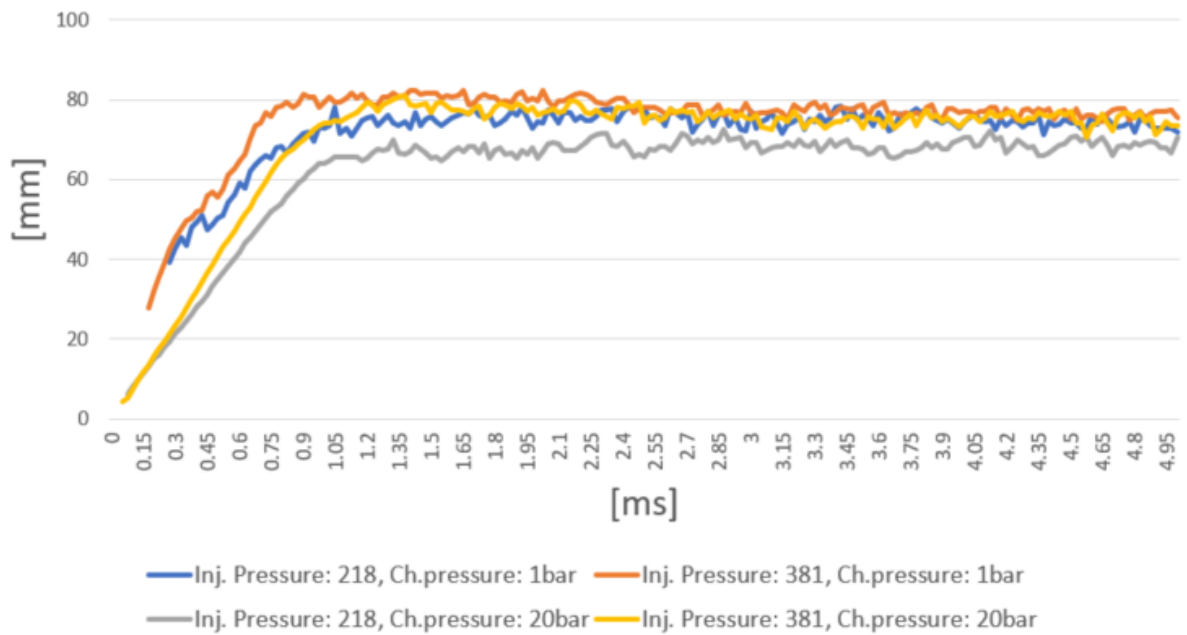
Penetratrion length, triple nozzle

Legend:
— Inj. Pressure: 218, Ch.pressure: 1bar — Inj. Pressure: 381, Ch.pressure: 1bar
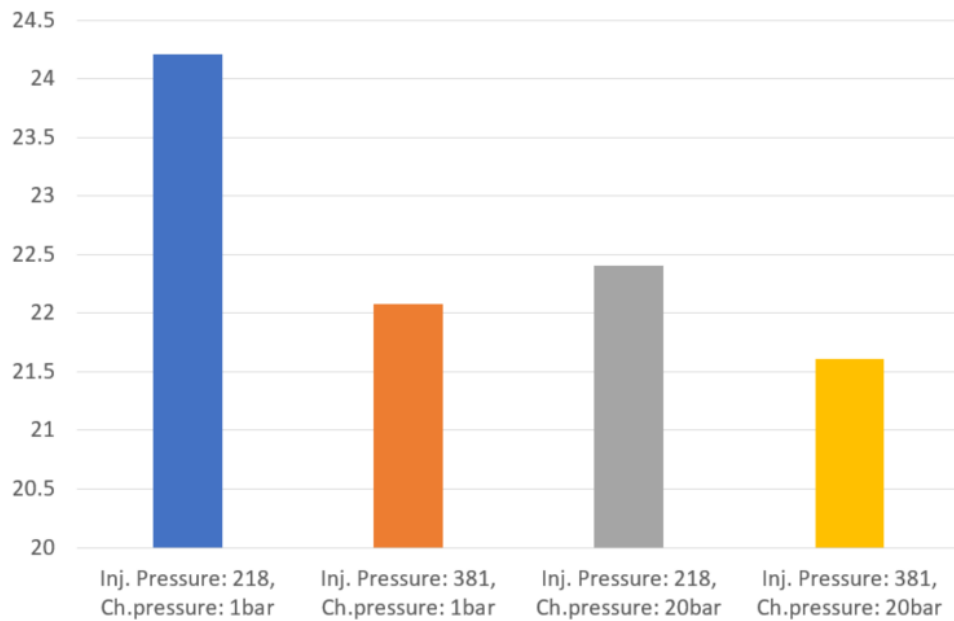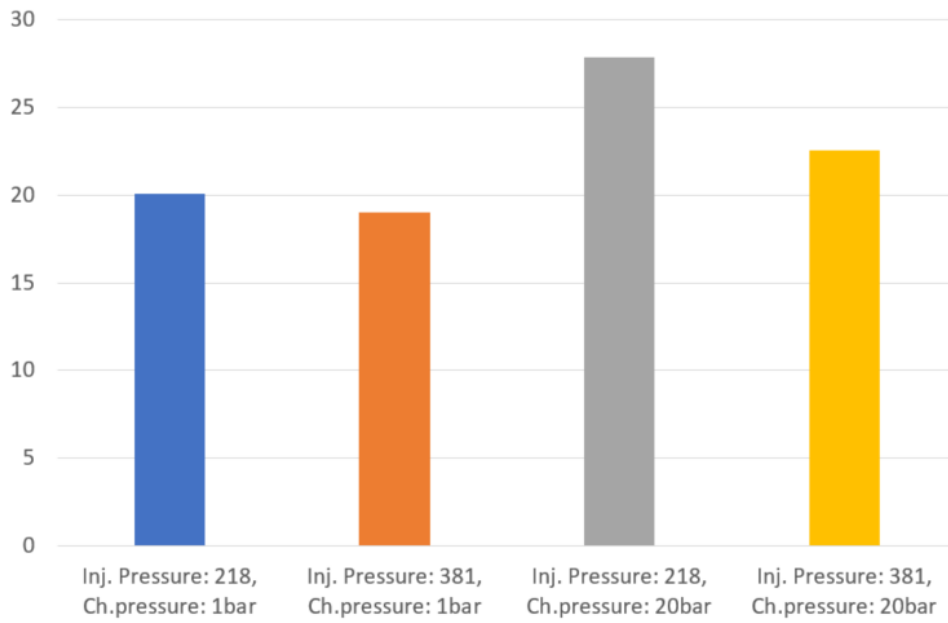— Inj. Pressure: 218, Ch.pressure: 20bar — Inj. Pressure: 381, Ch.pressure: 20bar
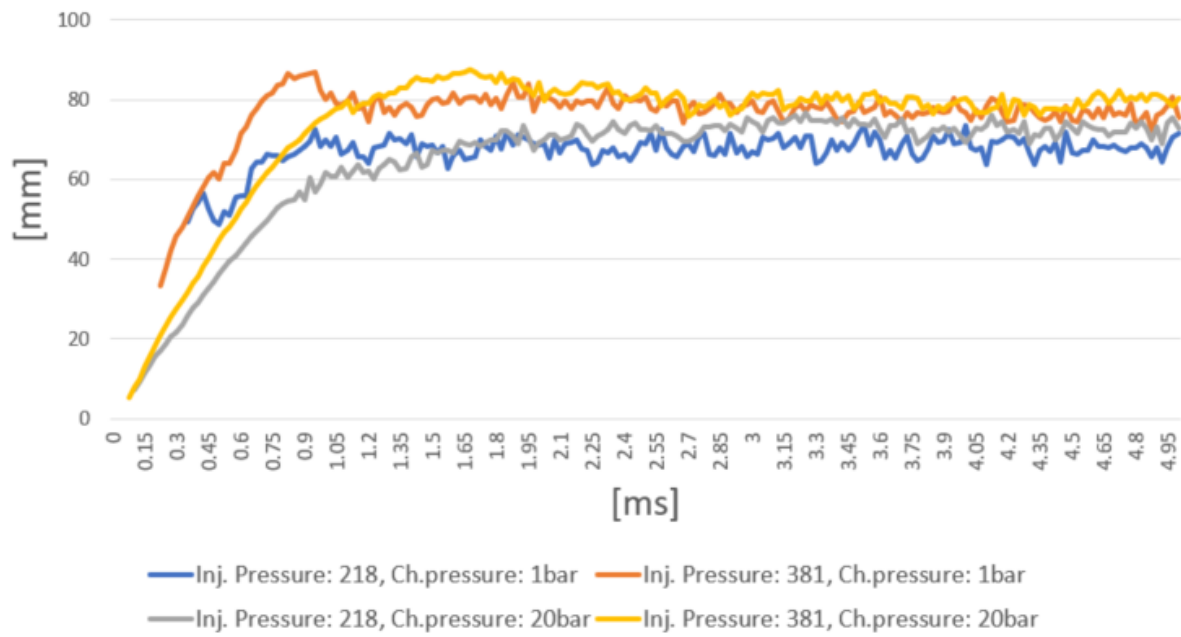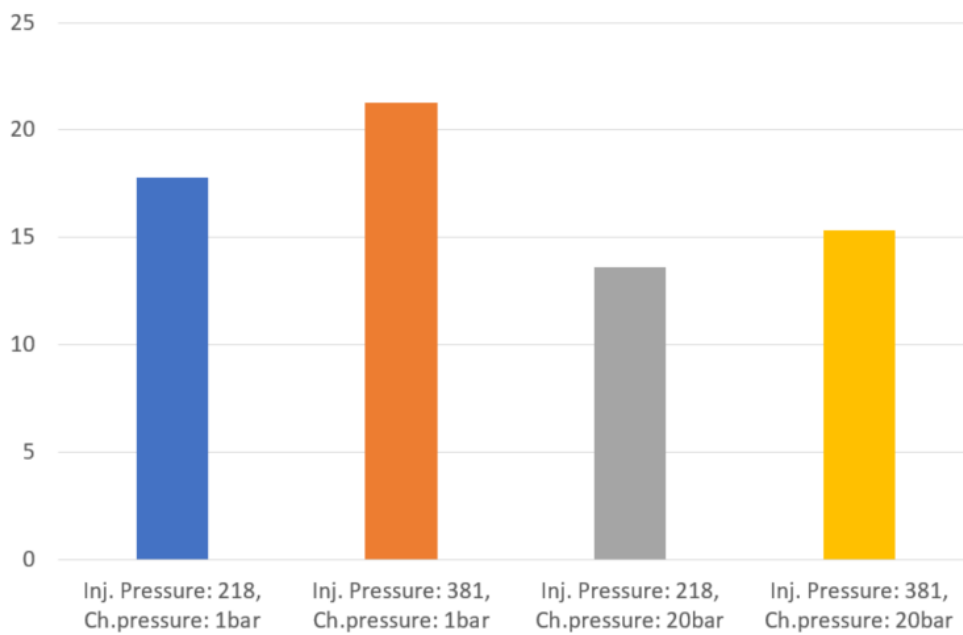
Appendix F: Gas Jet Cone Angles
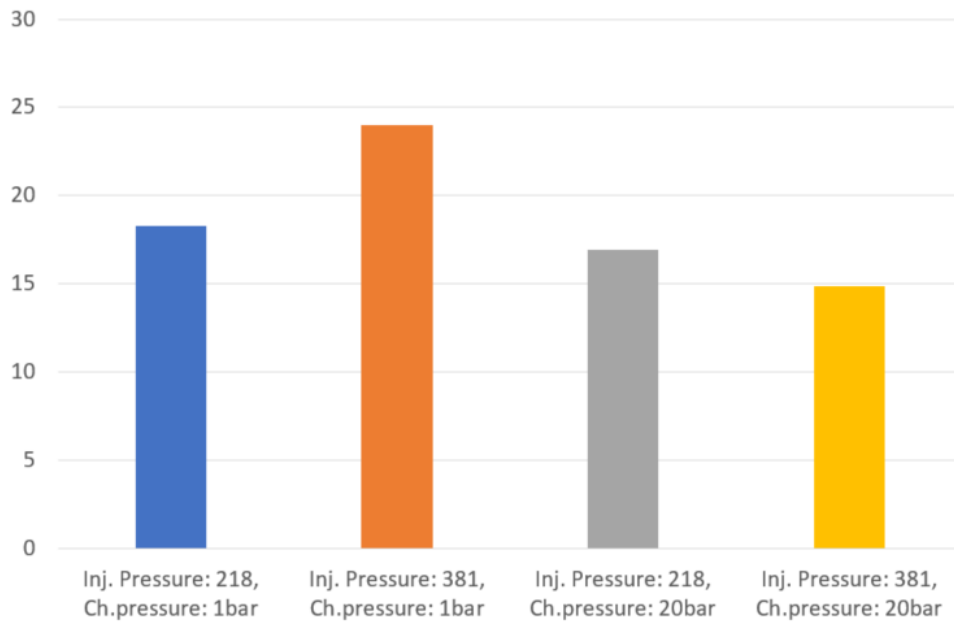
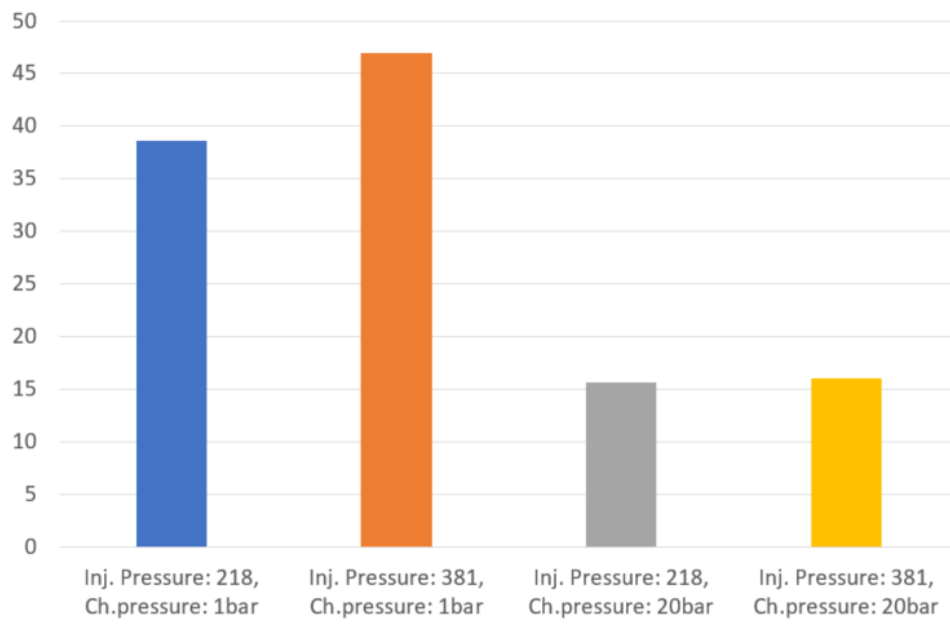**Figure 9.2.1:** Cone angle. 1.48mm circular nozzle

Figure 9.2.2: Cone angle. 2.04mm circular nozzle

Figure 9.2.3: Cone angle. 2.88mm circular nozzle

Figure 9.2.4: Cone angle. Double nozzle

Figure 9.2.5: Cone angle. Triple nozzle